

Theoretical and Experimental Investigation of Bidisperse Particle-Laden Flows on an Incline

Jessica Bojorquez, Adam Busis¹, Chutian Ma², Aviva Prins,
Andrew Shapiro, Qiya Zhu, and Xinzhe Zuo

¹Harvey Mudd College

² University of Science and Technology of China

PI: Dr. Andrea Bertozzi
Mentor: Dr. Claudia Falcon

Applied Mathematics REU
August 11, 2017
University of California, Los Angeles

Abstract

We investigate constant flux bidensity slurries and constant volume bidisperse slurries on an incline. The former mixture consists of two negatively buoyant particle species with the same diameter and different densities, while the latter slurry consists of a single negatively buoyant species of particle but with two distinct diameters. For all experiments, an interplay between two key forces, shear induced migration and gravitational settling, result in the formation of two distinct regimes, ridged and settled, and a third transient regime, well mixed. We develop theoretical models and simulations to compare against our experimental results, as well as produce a phase diagram for constant flux bidensity that can predict the long term regimes of slurries. Additionally, we observe an unexpected settling phenomenon in the bidisperse experiments where long term particle front order is the opposite of what we expect. At first, the large particles settle out of the flow, however we observe that with enough time, the larger particle front migrates in front of the smaller particle front, indicating that the larger particles do not completely sink.

Contents

1	Introduction	3
2	Theory	4
2.1	Bidensity Constant Flux Model	4
2.2	Bidisperse Constant Volume Model	11
3	Experimental Procedure	14
3.1	Set Up	14
3.2	Data Analysis	16
4	Results	19
4.1	Bidensity	20
4.2	Bidisperse	29
5	Conclusion	33
6	Acknowledgements	33
Appendix A Toy Problem		35
Appendix B Concentration Measurements		37
Appendix C Landslide Erosion Experiments		38

1 Introduction

The study of particle-laden flow is important in many contexts, whenever flows with concentrations of immiscible particles occur. This occurs in many fields, such as environmental (mud slides), industrial (heat transfer processes; coating processes), and biological contexts (food transport), and are of particular interest to mining, paper, and pharmaceutical industries. Previous research has been done on one and two species of particles suspended in viscous fluid, i.e. a slurry, flowing down a straight incline.

Previous research has revealed general properties about particle-laden flow, which undergoes two forces. Huppert [1] investigated a gravity-driven clear-fluid model, and found that the flow grows $\sim t^{1/3}$. Leighton and Acrivos [2] used a thin-gap Couette viscometer and developed a model for a single species particle interaction, introducing the idea of shear-induced migration due to irreversible interparticle interactions. Phillips [3] further developed the model for monodisperse in Couette device by producing a constitutive equation to find particle concentration distribution and velocity fields. He also experimentally determined two constants K_c and K_v for particle fluxes caused by shear-induced migration. Cook [4] incorporated shear induced migration into the mathematical model of particle flux for monodisperse suspensions.

The competing forces of gravity and shear force cause the emergence of three different regimes. In the ridged regime, the shear forces are dominant, causing particles to be suspended and pushed towards the front of the flow. In the settled regime, the gravitational force is dominant, causing the particles to sink [5]. Finally, Murisic et al. [6] established a model for the transient well-mixed regime. An analytic solution is derived for the dilute approximation and the exact solution predicts the presence of the two-front configuration. However, this paper assumes that the particle equilibrates quickly in the z -direction, and does not give a detailed explanation on the motion of particles in the z -direction. We investigate this assumption in Appendix A. Previous research has classified these regimes for bidensity particle-laden flows with constant volume initial conditions [7, 8].

This summer, we investigate the emergence of these regimes for bidensity particle laden flows with constant flux initial conditions. Our experiments focus on determining the effect of not only angles but also particle volume ratio. We construct a phase diagram with respect to angle and volume ratio and determine critical points between settled regime and ridged regime, which can be compared to the phase diagram in [8]. We also document the thickness of the flow over distance. In theory, we extend the bidensity, constant volume model in [7] to our bidensity, constant flux situation. We modify the initial condition, extending the initial value of height to the entire negative half x -axis to meet the constant flux condition.

We also study bidisperse, constant volume flow. Murisic et al. performed monodisperse experiments with different diameters. Murisic et al. conclude that particle size plays no role in expected regimes, rather it affects the time at which the regimes are formed [5]. The research by Gladstone et al. indicates that the ratio of large to small beads have a significant effect on the characteristics of the slurry, so we test multiple ratios [9]. In this situation we cannot directly inherit the model from [7]. We modify the terms for the shear-induced migration of particles to take into account the different diameters of the particles in particle-particle interactions. We also change the maximum packing fraction of the particles, which is a function of the relative concentration of particles when there are two different sizes

[10].

Finally, we develop a new technique to measure concentration of particles along the track (see Appendix B). We also run experiments to compare to recent simulations of landslide erosion and dam breaks (see Appendix C) [11].

2 Theory

In this section, we develop mathematical models for bidensity constant flux and bidisperse constant volume. In our models, we have an incline with an adjustable angle α . Figure 1 shows the x -, y -, and z -coordinates' directions, as well as the direction of the gravity vector g . A well-mixed slurry flows down the incline. Since the slurry behaves symmetrically in y -direction, only x - and z -directions matter in our case.

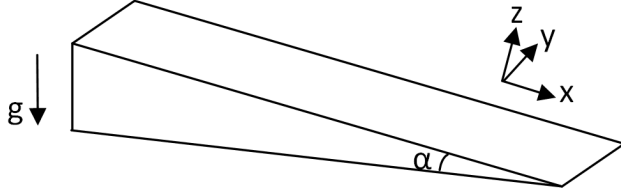


Figure 1: Schematic of Incline

2.1 Bidensity Constant Flux Model

Wong et al. [7] developed a diffusive flux model for bidensity constant volume, and they compared experimental and theoretical height profile and front positions. We adapt their diffusive flux model but change the initial and left boundary conditions to represent constant flux, and similarly, we produce simulations to compute height profile and front positions.

We mix two negatively buoyant particles of same diameter d but different densities ρ_1 and ρ_2 in a fluid with large viscosity μ_l and density ρ_l so that $\rho_l < \rho_1 < \rho_2$. The slurry is then poured by a pump with constant flow rate Q . We define ϕ_i , $i = 1, 2$ to be the volume fraction of particle i to the total volume, $\phi = \phi_1 + \phi_2$, and they are functions of x, z and time t . The mixture is Newtonian, and its effective viscosity is given by Krieger-Dougherty relation $\mu(\phi) = \mu_l(1 - \phi/\phi_{max})^{-2}$, where ϕ_{max} is the maximum packing fraction. Its effective density $\rho(\phi) = (1 - \phi)\rho_l + \phi_1\rho_1 + \phi_2\rho_2$. When the slurry flows down the incline, it has a velocity vector \mathbf{u} of x, z components $\mathbf{u} = (u, w)$.

Before modeling the height and front positions, we need some preparation steps. We first look at two basic equations governing the fluid and particle motion. The first are the Navier-Stokes equations (1) and the second is derived from particle mass conservation (2),

$$\rho \frac{\partial \mathbf{u}}{\partial t} + \rho \mathbf{u} \cdot \nabla \mathbf{u} = \nabla \cdot (-pI + \mu(\nabla \mathbf{u} + \nabla \mathbf{u}^T)) + \rho \mathbf{g} \quad (1)$$

$$0 = \frac{\partial \phi_i}{\partial t} + \mathbf{u} \cdot \nabla \phi_i + \nabla \cdot \mathbf{J}_i, \quad i = 1, 2. \quad (2)$$

Here, the \mathbf{J}_i term is the flux of particle i , and it is also a vector with x - and z -components. Since the fluid has a small Reynolds number, the momentum terms in (1) can be ignored, so the equations (1) become

$$0 = \nabla \cdot (-pI + \mu(\nabla \mathbf{u} + \nabla \mathbf{u}^T)) + \rho \mathbf{g}. \quad (3)$$

The two equations can be further simplified after nondimensionalization and thin film approximation. We use the scales for nondimensionalization suggested in [7],

$$(x, z) = H\left(\frac{1}{\varepsilon}\hat{x}, \hat{z}\right), \quad (u, w) = U(\hat{u}, \varepsilon\hat{w})$$

$$p = \frac{U\mu_l}{H}\hat{p}, \quad (J_i^x, J_i^z) = \frac{d^2 U}{H^2}(\varepsilon\hat{J}_i^x, \hat{J}_i^z),$$

where $U = H^2\rho_l g \sin \alpha / \mu_l$ and $\varepsilon \ll 1$. Note the symbols with hats above are the nondimensionalized variables. If we only look at the x -component of (3), we have

$$0 = -\frac{\partial p}{\partial x} + 2\frac{\partial}{\partial x} \left(\mu \frac{\partial u}{\partial x} \right) + \frac{\partial}{\partial z} \left(\mu \frac{\partial u}{\partial z} + \mu \frac{\partial w}{\partial x} \right) + \rho g \sin \alpha.$$

If we nondimensionalize the equation, we can get the leading order of ε for each term. The only terms containing ε are $w, \frac{\partial}{\partial x}$, each with order 1. The orders calculated are marked as below

$$0 = -\frac{\partial p^1}{\partial x} + 2\frac{\partial}{\partial x} \left(\mu \frac{\partial u^2}{\partial x} \right) + \frac{\partial}{\partial z} \left(\mu \frac{\partial u^0}{\partial z} + \mu \frac{\partial w^2}{\partial x} \right) + \rho g \sin \alpha^0.$$

Since $\varepsilon \ll 1$, only the 0 order terms matter, i.e.

$$0 = \frac{\partial}{\partial z} \left(\mu \frac{\partial u}{\partial z} \right) + \rho g \sin \alpha. \quad (4)$$

We nondimensionalize the equation with u, z stated as before, $\mu = \mu_l \hat{\mu}$, $\rho = \rho_l \hat{\rho}$. What we get is $(\mu u_z)_z = -\rho$; here the hats are dropped for brevity. As shear stress $\sigma = \mu(\phi)\frac{\partial u}{\partial z}$, the equation is just

$$\frac{\partial \sigma}{\partial z} = -\rho. \quad (5)$$

Equation (2) can be nondimensionalized in a similar way. We again mark the leading order of ε for each term,

$$0 = \frac{\partial \phi_i^1}{\partial t} + u \frac{\partial \phi_i^1}{\partial x} + w \frac{\partial \phi_i^1}{\partial z} + \frac{\partial J_i^x^2}{\partial x} + \frac{\partial J_i^z^0}{\partial z}.$$

The only term with order 0 gives us $\frac{\partial J_i^z}{\partial z} = 0$, but there is a $\frac{d^2}{H^2}$ factor after nondimensionalization. To make our simplification legitimate, we need the assumption that $\varepsilon \ll (\frac{d}{H})^2 \ll 1$. Since we cannot have the particles keep going up or down in the z -direction with a constant

rate, what this nondimensionalization suggests is that the particles are in equilibrium in z -direction, i.e.

$$J_i^z = 0, i = 1, 2. \quad (6)$$

To remove the dependence on the film height $h(x, t)$, we use the scaled variable $s = \frac{z}{h}$, and the scaled quantities $\tilde{\sigma}(x, s, t) = h^{-1}\sigma(x, hs, t)$, $\tilde{\phi}(x, s, t) = \phi(x, sh, t)$ as stated in [7]. We then derive

$$\begin{aligned} \frac{\partial \tilde{\sigma}}{\partial s} &= \frac{\partial}{\partial s} \left(\frac{\sigma(x, hs, t)}{h} \right) = \frac{1}{h} \frac{\partial \sigma}{\partial z} h = \frac{\partial \sigma}{\partial z} = -\frac{\rho}{\rho_l} \\ &= -\frac{1}{\rho_l} ((1 - \phi)\rho_l + \phi_1\rho_1 + \phi_2\rho_2) \\ &= \phi - 1 - \phi_1 \frac{\rho_1}{\rho_l} - \phi_2 \frac{\rho_2}{\rho_l} \\ &= -1 - \phi_1 \left(\frac{\rho_1}{\rho_l} - 1 \right) - \phi_2 \left(\frac{\rho_2}{\rho_l} - 1 \right) \\ &= -1 - \tilde{\phi}\rho(\tilde{\chi}) \end{aligned} \quad (7)$$

if we define $\tilde{\chi} = \frac{\tilde{\phi}_1}{\tilde{\phi}}$, $\rho_{s1} = \frac{\rho_1 - \rho_l}{\rho_l}$, $\rho_{s2} = \frac{\rho_2 - \rho_l}{\rho_l}$, $\rho(\tilde{\chi}) = \rho_{s1}\tilde{\chi} + \rho_{s2}(1 - \tilde{\chi})$.

Now we look at the diffusive flux model in [7], which includes settling, shear-induced diffusion and mixing of particles:

$$\begin{aligned} \mathbf{J}_i &= \mathbf{J}_{\text{settling},i} + \mathbf{J}_{\text{shear},i} + \mathbf{J}_{\text{tracer},i}, \\ \mathbf{J}_{\text{shear},i} &= -\frac{d^2 K_c \phi_i}{4} \nabla(\dot{\gamma}\phi) - \frac{d^2}{4} \frac{K_v \dot{\gamma} \phi \phi_i}{\mu(\phi)} \nabla \mu(\phi), \\ \mathbf{J}_{\text{settling},i} &= \frac{d^2 \mathbf{g} \phi_i}{18 \mu_l} \left(M_0 (\rho_i - \rho_l) + M_I \sum_{j=1}^2 (\rho_j - \rho_l) \frac{\phi_j}{\phi} \right), \\ \mathbf{J}_{\text{tracer},i} &= -\frac{\dot{\gamma} d^2}{4} D_{tr}(\phi) \phi \nabla \left(\frac{\phi_i}{\phi} \right), \end{aligned}$$

where $K_c \approx 0.41$ and $K_v \approx 0.62$ are experimentally determined constants [3], $\dot{\gamma}$ is the shear rate, $M_0 = 1 - \frac{\phi}{\phi_m}$, $M_I = \frac{1 - \phi}{\mu} - M_0$, and we use the expression $D_{tr}(\phi) = \frac{1}{2} \phi^2 (1 + 0.09 e^{7\phi})$ in [12].

Use (6), we have

$$\begin{aligned} 0 = J_i^z &= -\frac{d^2 K_c \phi_i}{4} \nabla(\dot{\gamma}\phi) - \frac{d^2}{4} \frac{K_v \dot{\gamma} \phi \phi_i}{\mu(\phi)} \nabla \mu(\phi) \\ &\quad - \frac{d^2 g \cos \alpha \phi_i}{18 \mu_l} \left(M_0 (\rho_i - \rho_l) + M_I \sum_{j=1}^2 (\rho_j - \rho_l) \frac{\phi_j}{\phi} \right) - \frac{\dot{\gamma} d^2}{4} D_{tr}(\phi) \phi \nabla \left(\frac{\phi_i}{\phi} \right). \end{aligned}$$

If we add J_1^z and J_2^z and do a simplification, we have

$$\phi(\dot{\gamma}\phi)_z + \frac{K_v}{K_c} \frac{\dot{\gamma}\phi^2}{\mu(\phi)} (\mu(\phi))_z + \frac{2g \cos \alpha}{9K_c \mu_l} \left(M_0(\phi_1 \rho_1 + \phi_2 \rho_2 - \phi \rho_l) + \phi M_I \sum_{j=1}^2 (\rho_j - \rho_l) \frac{\phi_j}{\phi} \right) = 0. \quad (8)$$

We look at $(\dot{\gamma}\phi)_z$ first, we know $\dot{\gamma} = \frac{\sigma}{\mu}$, so use product rule and (7),

$$\left(\frac{\sigma}{\mu} \phi \right)_z = \phi \left(-\frac{\rho}{\rho_l} \frac{1}{\mu} - \sigma \frac{1}{\mu^2} \mu_z \right) + \frac{\sigma}{\mu} \phi_z,$$

Using the relation $\mu(\phi) = \mu_l \left(1 - \frac{\phi}{\phi_m} \right)^{-2}$ (here ϕ_m is just ϕ_{max}), we can find μ_z :

$$\mu_z = -2\mu_l \left(1 - \frac{\phi}{\phi_m} \right)^{-3} \left(-\frac{\phi_z}{\phi_m} \right) = 2\mu \left(1 - \frac{\phi}{\phi_m} \right)^{-1} \frac{\phi_z}{\phi_m} = 2\mu \phi_z (\phi_m - \phi)^{-1}.$$

Hence, the first term in (8) becomes

$$\phi(\dot{\gamma}\phi)_z = -\frac{\rho}{\rho_l} \frac{\phi^2}{\mu} - 2\frac{\sigma\phi^2}{\mu} (\phi_m - \phi)^{-1} \phi_z + \frac{\sigma\phi}{\mu} \phi_z.$$

Replace $\dot{\gamma}$ by $\frac{\sigma}{\mu}$ and μ_z by the expression we just got, the second term in (8) becomes $2\frac{K_v}{K_c} \frac{\sigma\phi^2}{\mu} (\phi_m - \phi)^{-1} \phi_z$. Let $c_1 = 2(K_v/K_c - 1)$, combine the first two terms, we have

$$\frac{\sigma\phi}{\mu} (\phi_m - \phi)^{-1} (\phi_m - \phi + c_1 \phi) \phi_z - \frac{\rho}{\rho_l} \frac{\phi^2}{\mu}.$$

The third term in (8) can be simplified as

$$\begin{aligned} & M_0(\phi_1 \rho_1 + \phi_2 \rho_2 - \phi \rho_l) + \phi M_I \sum_{j=1}^2 (\rho_j - \rho_l) \frac{\phi_j}{\phi} \\ &= \rho_l \left(M_0 \phi \left(\frac{\phi_1}{\phi} \frac{\rho_1}{\rho_l} + \frac{\phi_2}{\phi} \frac{\rho_2}{\rho_l} - 1 \right) + \phi M_I \sum_{j=1}^2 \left(\frac{\rho_j}{\rho_l} - 1 \right) \frac{\phi_j}{\phi} \right) \\ &= \rho_l (M_0 \phi \rho(\chi) + \phi M_I \rho(\chi)) \\ &= \phi \frac{1 - \phi}{\mu} \rho(\chi). \end{aligned}$$

Put all what we have and divide by $\frac{\phi}{\mu}$, (8) turns

$$\frac{\sigma(\phi_m - \phi + c_1 \phi)}{\phi_m - \phi} \frac{\partial \phi}{\partial z} - \frac{\rho}{\rho_l} \phi + \frac{2g \cos \alpha}{9K_c \mu_l} (1 - \phi) \rho(\chi) = 0.$$

Then we try to nondimensionalize and use scaled quantities, in particular $\mu_l = 1$, $g \cos \alpha = \cot \alpha$, and $\frac{\partial \tilde{\phi}}{\partial s} = h \frac{\partial \phi}{\partial z}$, which helps make σ into $\tilde{\sigma}$,

$$\frac{\tilde{\sigma}(\phi_m - \tilde{\phi} + c_1 \tilde{\phi})}{\phi_m - \tilde{\phi}} \frac{\partial \tilde{\phi}}{\partial s} + (-1 - \tilde{\phi} \rho(\tilde{\chi})) \tilde{\phi} + B(1 - \tilde{\phi}) \rho(\tilde{\chi}) = 0$$

where $B = \frac{2 \cot \alpha}{9K_c}$. Reorder the terms, we have

$$\frac{\partial \tilde{\phi}}{\partial s} = \frac{(\phi_m - \tilde{\phi})(\tilde{\phi} + \rho(\tilde{\chi})(\tilde{\phi}^2 - B(1 - \tilde{\phi})))}{\tilde{\sigma}(\phi_m - \tilde{\phi} + c_1 \tilde{\phi})} \quad (9)$$

We can get another ODE for $\tilde{\chi}$ in a similar way if we use $\frac{J_1^z}{\phi_1} - \frac{J_2^z}{\phi_2}$. The equation derived is,

$$\frac{\partial \tilde{\chi}}{\partial s} = c_2 \frac{1}{\tilde{\sigma}} \frac{1}{D_{tr}(\tilde{\phi})} \tilde{\chi}(1 - \tilde{\chi}) \frac{\phi_m}{\phi_m - \tilde{\phi}} \quad (10)$$

where $c_2 = -\frac{2 \cot \alpha}{9} (\rho_1 - \rho_2)$.

Up to this point, we have a system of three coupled first order ODEs from (7)(9)(10),

$$\begin{cases} \frac{\partial \tilde{\sigma}}{\partial s} = -1 - \tilde{\phi} \rho(\tilde{\chi}) \\ \frac{\partial \tilde{\phi}}{\partial s} = \frac{(\phi_m - \tilde{\phi})(\tilde{\phi} + \rho(\tilde{\chi})(\tilde{\phi}^2 - B(1 - \tilde{\phi})))}{\tilde{\sigma}(\phi_m - \tilde{\phi} + c_1 \tilde{\phi})} \\ \frac{\partial \tilde{\chi}}{\partial s} = c_2 \frac{1}{\tilde{\sigma}} \frac{1}{D_{tr}(\tilde{\phi})} \tilde{\chi}(1 - \tilde{\chi}) \frac{\phi_m}{\phi_m - \tilde{\phi}} \end{cases}$$

with a boundary condition $\tilde{\sigma}(1) = 0$ based on stress-balance on the free surface. However, we cannot directly use this boundary condition as we have $\tilde{\sigma}$ on the denominator in our equations. To deal with this,

$$\int_0^1 \frac{\partial \sigma}{\partial s} ds = \sigma(1) - \sigma(0) = \int_0^1 -1 - \tilde{\phi} \rho(\tilde{\chi}) ds,$$

from which we get

$$\sigma(0) = 1 + \rho_{s2} \int_0^1 \tilde{\phi} ds + (\rho_{s1} - \rho_{s2}) \int_0^1 \tilde{\phi} \tilde{\chi} ds \quad (11)$$

as our initial condition. We need two more constraints for the coupled ODEs, which we only have in integral form,

$$\int_0^1 \tilde{\phi} ds = \bar{\phi}, \quad \int_0^1 \tilde{\phi} \tilde{\chi} ds = \bar{\phi}_1,$$

where $\bar{\phi}$ and $\bar{\phi}_1$ are depth-averaged concentrations of total particles and particle 1. Moreover, we define $\bar{\chi} = \bar{\phi}_1 / \bar{\phi}$. We use the shooting method to apply these two integral constraints.

The basic idea is that we guess initial conditions for $\tilde{\chi}$ and $\tilde{\phi}$ so that we have an initial value problem, which can be solved using Matlab's builtin ODE solver `ode15s`. We then perform numerical integration for $\tilde{\phi}$ and $\tilde{\phi}\tilde{\chi}$ and compare the values with $\bar{\phi}$ and $\bar{\phi}\bar{\chi}$. Finally, we use `fminsearchbnd` to find the optimal initial conditions which produce the smallest sum of difference squares. Then our numerical solution to the system is what we get for the IVP with the optimal initial conditions.

Once we have the solutions of $\tilde{\sigma}$, $\tilde{\chi}$, and $\tilde{\phi}$ for given $\bar{\phi}$ and $\bar{\chi}$, we can compute the average fluxes in the x -direction of the fluid and particles 1 and 2, denoted respectively by f , g_1 , and g_2 . The definitions for f and g_i are

$$f(\bar{\phi}, \bar{\chi}) = \int_0^1 \tilde{u} ds, \quad g_i(\bar{\phi}, \bar{\chi}) = \int_0^1 \tilde{u}\tilde{\phi}_i ds,$$

where $\tilde{u}(x, s, t) = \int_0^s \mu(\tilde{\phi}(x, w, t))^{-1} \tilde{\sigma}(x, w, t) dw = \int_0^s \left(1 - \frac{\tilde{\phi}}{\phi_m}\right)^2 \tilde{\sigma} dw$. The function `cumtrapz` can integrate numerically to get \tilde{u} , and we use `trapz` to integrate \tilde{u} and $\tilde{u}\tilde{\phi}_i$ to find f and g_i .

Now, we are prepared to get the height profile and front position. From conservation of fluid and particle mass, we derive the following system of PDEs,

$$\begin{aligned} 0 &= \frac{\partial h}{\partial t} + \frac{\partial}{\partial x}(h^3 f(\bar{\phi}, \bar{\chi})), \\ 0 &= \frac{\partial(h\bar{\phi}_i)}{\partial t} + \frac{\partial}{\partial x}(h^3 g_i(\bar{\phi}, \bar{\chi})), \quad i = 1, 2. \end{aligned}$$

We can express the system in vector notation by setting $U = (h, h\bar{\phi}_1, h\bar{\phi}_2)^T$ and $F(U) = h^3(f, g_1, g_2)^T$, and have

$$\frac{\partial U}{\partial t} + \frac{\partial}{\partial x}(F(U)) = 0. \quad (12)$$

If we approximate the partial derivatives using forward-time backward-space finite difference scheme, we have (12) rewritten as

$$\frac{U_m^{n+1} - U_m^n}{k} + \frac{F(U_m^n) - F(U_{m-1}^n)}{h} = 0,$$

where U_m^n denotes U at position step m and time step n , k is the time increment, and h is the position increment. If we reorder the terms, we have

$$U_m^{n+1} = U_m^n - \lambda(F(U_m^n) - F(U_{m-1}^n)),$$

where $\lambda = k/h$.

In order to use the upwind scheme, we need to find suitable initial and left boundary conditions to represent constant flux. Our pump has a constant flow rate Q in units m^3/s , and the track has width W . For the initial conditions, we assume there is no particle for $x > 0$ but only a very thin precursor film of height ε . For $x < 0$, we have a well-mixed slurry with ϕ_0, χ_0 and a constant height H which is just the characteristic height we use for

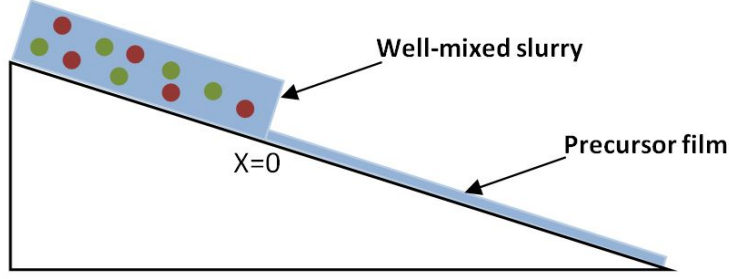


Figure 2: Initial Conditions for Constant Flux

nondimensionalization and can be calculated using Q , W , ϕ_0 and χ_0 . Figure 2 gives a visual understanding of the initial conditions.

To calculate H , we use the fact that $Q = \int_0^W \int_0^H u(z) dz dy$. Here u is the x -direction speed of the fluid at time $t = 0$ and any arbitrary position $x < 0$. Since u is constant along the y direction, the double integral becomes a single one, and if we recall the nondimensionalization used for u , we get

$$Q = \frac{WH^2 \rho_l g \sin \alpha}{\mu_l} \int_0^H \hat{u}(z) dz.$$

If we further apply the scaled variable \tilde{u} ,

$$Q = \frac{WH^3 \rho_l g \sin \alpha}{\mu_l} \int_0^1 \tilde{u}(s) ds.$$

As $\tilde{\sigma} = \frac{\mu(\phi_0)}{\mu_l} \frac{\partial \tilde{u}}{\partial s}$, and we have the no-slip boundary condition at $s = 0$, we have

$$\tilde{u}(s) = \frac{\mu_l}{\mu(\phi_0)} \int_0^s \tilde{\sigma}(w) dw.$$

Use the ODE (7) we derived for $\tilde{\sigma}$,

$$\tilde{\sigma}(w) - \tilde{\sigma}(0) = \int_0^w -1 - \phi_0 \rho(\chi_0) dv,$$

and also recall (11) such that $\tilde{\sigma}(0) = 1 + \phi_0 \rho(\chi_0) = \frac{\rho(\phi_0)}{\rho_l}$ in this case. If we substitute all these, we have

$$Q = \frac{WH^3 g \sin \alpha \rho(\phi_0)}{3\mu(\phi_0)},$$

from which we get

$$H = \left[\frac{3\mu(\phi_0)Q}{W\rho(\phi_0)g \sin \alpha} \right]^{1/3}.$$

We can write the initial conditions in step-function format,

$$h(x, 0) = \begin{cases} \left[\frac{3\mu(\phi_0)Q}{W\rho(\phi_0)g \sin \alpha} \right]^{1/3}, & x \leq 0 \\ \varepsilon, & x > 0 \end{cases}$$

$$\bar{\phi}(x, 0) = \begin{cases} \phi_0, & x \leq 0 \\ 0, & x > 0 \end{cases} \quad \bar{\chi}(x, 0) = \begin{cases} \chi_0, & x \leq 0 \\ 0, & x > 0 \end{cases}$$

The left boundary condition is the same as the part of initial conditions for $x \leq 0$, as constant flux means a constant rate of slurries flowing down the incline so that the film height at $x = 0$ remains constant all the time.

Once we have these initial and left boundary conditions, we can build our grid of U forward in time. For each time step, we draw information from the previous time step. Although the f , g_1 , g_2 in $F(U)$ can be calculated using $\bar{\phi}$ and $\bar{\chi}$, which are provided in U , if we compute them as we run the finite difference scheme, it takes a long time. A more efficient way is to create flux tables where we compute values of f , g_1 and g_2 beforehand for some discrete value of $\bar{\phi}$ and $\bar{\chi}$. Then when solving for U , we use interpolation to get f , g_1 and g_2 for a particular set of $\bar{\phi}$ and $\bar{\chi}$ if it has not been computed previously.

After we solve the PDE system, we have values of h , $\bar{\phi}$ and $\bar{\chi}$. The height profile can be easily gained from h . We can also get the evolution of the front positions over time. The fluid front is easy to determine from the height profile. We search from the end and go backwards in position until the point where the gradient of h is greater than 0. The lighter particle front position is defined as the point where both $\bar{\phi}_1$ and $\bar{\phi}_2$ reach 0, as from that point onward, there are no particles in the slurry. Similarly, we define the heavier particle front to be the point where $\bar{\phi}_2$ reaches 0. If we define in this way, there is a small problem. Behind the heavier particle front, there are still lighter particles present, so instead of only having heavier particles, we have a mixture of two particles. However, this is best definition we can come up now for the simulation purpose.

2.2 Bidisperse Constant Volume Model

To create a model for the bidisperse system, we modify the model in [7]. In this model, the particles are assumed to first assumed to reach equilibrium in the z -direction, and then the flow rate in the x -direction is determined based on the z -distribution. The parts of the model that depend on the diameter of the particles are the z -fluxes J_{shear} , $J_{settling}$, and J_{tracer} , so we modify these fluxes to create our bidisperse model.

For bidensity, the shear term for particle 1 is given by

$$-a^2 K_c \phi_i \nabla (\dot{\gamma} \phi) - a^2 K_v \dot{\gamma} \phi \phi_i \frac{\nabla \mu}{\mu}.$$

As explained in [3], this model as being caused by interactions between particle 1 and all other particles, with the characteristic length of each interaction proportional to the radius a .

If instead we have two different sizes of particles, then these terms will be different depending on which size of particle it interacts with. Suppose that we want to know the flux of particles of radius a_1 . Then the flux caused by interactions with other particles of radius a_1 should be proportional to $a_1^2 \nabla(\dot{\gamma}\phi_1)$. The length scale of interactions between particles of radius a_1 and those of radius a_2 , though, is given by an average radius \hat{a} which we take to be $\sqrt{a_1 a_2}$. So the flux of particle 1 caused by interactions with particle 2 is proportional to $\hat{a}^2 \nabla(\dot{\gamma}\phi_2)$. This gives a total flux for particle 1 of

$$K_c \phi_1 (a_1^2 \nabla(\dot{\gamma}\phi_1) + \hat{a}^2 \nabla(\dot{\gamma}\phi_2)) = K_c \phi_1 \nabla(\dot{\gamma}(a_1^2 \phi_1 + \hat{a}^2 \phi_2)).$$

We can let $\eta_1 = a_1^2 \phi_1 + \hat{a}^2 \phi_2$; then we have the flux equal to $K_c \phi_1 \nabla(\dot{\gamma}\eta_1)$. Similarly, for ϕ_2 , if we let $\eta_2 = \hat{a}^2 \phi_1 + a_2^2 \phi_2$, we get a flux of $K_c \phi_2 \nabla(\dot{\gamma}\eta_2)$. This is the same as the bidensity case, but now $a^2 \phi$ has been replaced by η_i . We can use the same reasoning for the viscosity gradient flux term, replacing the $a^2 \phi$ in that term with $a^2 \eta_i$, as well.

If we let the two densities of the particles be equal in the bidensity model, we get a settling term of

$$J_{\text{settling}} = -\frac{2a^2 \cot \alpha}{9} \rho_s \frac{1-\phi}{\mu}.$$

To modify this for different diameters, we replace a with a_i .

Finally, in the tracer diffusion term, this represents an exchange of the two types of particles in a situation where the net flux is 0. To preserve the property $J_{\text{tracer},1} + J_{\text{tracer},2} = 0$, we just replace a with \hat{a} and leave everything else the same.

This gives us the new flux equations

$$\begin{aligned} J_{\text{shear},i} &= -K_c \phi_i \nabla(\dot{\gamma}\eta_i) - K_v \dot{\gamma} \phi_i \eta_i \frac{\nabla \mu}{\mu} \\ J_{\text{settling},i} &= -\frac{2a_i^2 \cot \alpha}{9} \rho_s \frac{1-\phi}{\mu} \\ J_{\text{tracer},i} &= -\dot{\gamma} \hat{a}^2 D_{\text{tr}} \phi \nabla \left(\frac{\phi_i}{\phi} \right). \end{aligned}$$

There is one last thing we have to take into account. With two different sizes of particles, the maximum flux ϕ_m doesn't remain constant. As the relative concentration changes, ϕ_m also changes, and in general tends to be higher if there is more of a mixture of particles rather than just one or the other. We use the expression provided in [10]:

$$\phi_m = \phi_{m0} \left[1 + \frac{3}{2} |b|^{3/2} \left(\frac{\phi_1}{\phi} \right)^{3/2} \left(\frac{\phi_2}{\phi} \right) \right],$$

where $b = (a_1 - a_2)/(a_1 + a_2)$. From now on we will assume that $a_1 > a_2$.

To simplify this equation, we follow a lot of the same steps we did for the bidensity case. We want to put everything in terms of the three variables ϕ , X , and σ , where $\phi_1 = X\phi$, $\phi_2 = (1-X)\phi$, and $\dot{\gamma} = \sigma/\mu$.

First let's find the derivative of $\mu = \mu_l(1 - \phi/\phi_m)^{-2}$. We have

$$\frac{\partial \mu}{\partial z} = -2\mu_l(1 - \phi/\phi_m)^{-3} \left(-\frac{\phi'}{\phi_m} + \frac{\phi}{\phi_m^2} \phi'_m \right) = 2\mu_l(\phi - \phi_m)^{-1} \left(\phi' - \frac{\phi}{\phi_m} \phi'_m \right).$$

To find ϕ'_m , we differentiate logarithmically. We have

$$\phi_m - \phi_{m0} = \phi_{m0} \frac{3}{2} b^{3/2} X^{3/2} (1 - X),$$

so

$$\ln(\phi_m - \phi_{m0}) = 3/2 \ln X + \ln(1 - X) + C$$

where C is some constant. This gives us

$$\frac{\phi'_m}{\phi_m - \phi_{m0}} = \frac{3X'}{2X} - \frac{X'}{1 - X} = \frac{3 - 5X}{2X(1 - X)} X',$$

so

$$\phi'_m = (\phi_m - \phi_{m0}) \frac{3 - 5X}{2X(1 - X)} X'.$$

Therefore from before we have

$$\frac{\partial \mu}{\partial z} = 2\mu(\phi - \phi_m)^{-1} \left(\phi' - \frac{\phi}{\phi_m} (\phi_m - \phi_{m0}) \frac{3 - 5X}{2X(1 - X)} X' \right).$$

To save ourselves trouble, let

$$\zeta = \frac{\phi}{\phi_m} (\phi_m - \phi_{m0}) \frac{3 - 5X}{2X(1 - X)},$$

so that

$$\nabla \mu = 2\mu(\phi - \phi_m)^{-1}(\phi' - \zeta X').$$

Now we simplify

$$\begin{aligned} J_{shear,i} &= -K_c \phi_i \nabla(\dot{\gamma} \eta_i) - K_v \dot{\gamma} \eta_i \phi_i \frac{\nabla \mu}{\mu} \\ &= -\phi_i \left(K_c \nabla \left(\frac{\sigma \eta_i}{\mu} \right) + K_v \sigma \eta_i \frac{\nabla \mu}{\mu^2} \right) \\ &= -\frac{\phi_i}{\mu} \left(K_c \nabla(\sigma \eta_i) + (K_v - K_c) \sigma \eta_i \frac{\nabla \mu}{\mu} \right) \\ &= -\frac{\phi_i}{\mu} (K_c(\sigma \eta'_i + \sigma' \eta_i) + 2(K_v - K_c) \sigma \eta_i (\phi_m - \phi)^{-1}(\phi' - \zeta X')) \end{aligned}$$

Next we need to solve for σ' , X' , and ϕ' . The value for σ' is the same as it was in the bidensity case,

$$\sigma' = -1 - \phi \rho_s.$$

Rather than trying to solve for X' and ϕ' by hand, we use Maple to solve the system of equations

$$\begin{cases} J_{shear,1} + J_{settling,1} + J_{tracer,1} = 0 \\ J_{shear,2} + J_{settling,2} + J_{tracer,2} = 0 \end{cases}$$

for X' and ϕ' . After some simplification, the resulting equations are

$$X' = \frac{-BK_c\rho_s X(1-X)(1-\phi)(a_1-a_2)}{\bar{a}\sigma D_{tr}}$$

$$\phi' = \frac{\phi_m - \phi}{\bar{a}^2\sigma(\phi_m - \phi + c_1\phi)D_{tr}} \left[-(\phi\sigma'\bar{a}^2 + B\rho_s(1-\phi)\bar{A}^2)D_{tr} \right. \\ \left. + (a_1 - a_2)B\rho_sK_c\phi(1-\phi) \left((a_1 - a_2)X(1-X) - \bar{a}\frac{c_1}{\phi_m - \phi}\frac{\phi}{\phi_m}(\phi_m - \phi_{m0})\frac{3-5X}{2} \right) \right].$$

Here $B = 2 \cot \alpha / 9K_c$ as before, while \bar{a} and \bar{A} are given by

$$\bar{a} = a_1X + a_2(1-X)$$

$$\bar{A} = \sqrt{a_1^2X + a_2^2(1-X)}$$

One thing to note about this model is that X' is always negative. Since X represents the relative concentration of the larger particle, that means that the concentration of larger particles will decrease as we go up in the fluid; or, to rephrase, that the larger particles will tend to stay more near the bottom. This same behavior was found for a model of a bidisperse Couette flow of two particles of different diameters and similar densities in [10].

Once we have the expressions for the fluxes, we can continue to model the system using the same methods used to model the bidensity system.

3 Experimental Procedure

In order to test the diffusive flux model, we perform a number of experiments using a parametric study of relevance.

3.1 Set Up

The experimental apparatus (Figure 3) consists of the acrylic track we use for all of our experiments. The track is 90 cm in length and 14 cm in width. It has an adjustable angle of inclination, α . We perform two types of experiments on this track: bidensity experiments with the constant flux initial condition, and bidisperse experiments with the constant volume initial condition.

The liquid used in all experiments (Table 1) is polydimethylsiloxane (PDMS) oil with density $\rho_f = 0.971 \text{ g/cm}^3$ and kinematic viscosity $\nu = 10^{-3} \text{ m}^2/\text{s}$. The slurry is composed of two species of beads. For bidensity experiments, we use glass and ceramic beads with the same diameter (P3 and P4). For bidisperse experiments, we use pairs of beads with the same density but different diameters (P1 and P3, or P2 and P4). Since our beads are composed of the same material, we must dye the smaller beads for contrast. To do this, we mix the beads with food coloring and dry the mixture in a toaster oven. They are uniformly dyed and do not cluster together.

We perform a series of experiments varying the volume ratio between beads, χ and inclination angle, α , while keeping the total volume fraction ϕ_0 constant. Unlike in the

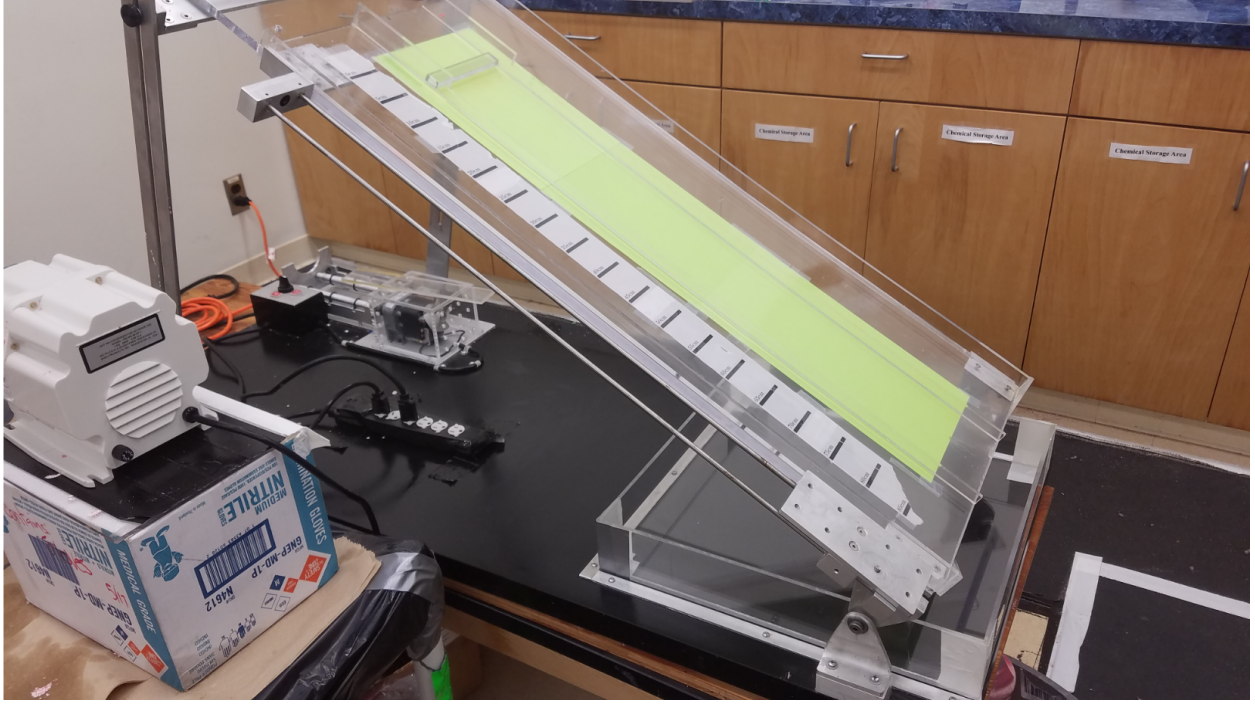


Figure 3: Picture of our experimental apparatus. The white pump to the left is used for constant flux experiments.

Table 1: Experimental parameters

Particles	density ρ	diameter d	color
Small Glass (P1)	2.5 g/cm ³	0.07 – 0.125 mm	pink (dyed)
Small Ceramic (P2)	3.8 g/cm ³	0.150 – 0.180 mm	blue (dyed)
Large Glass (P3)	2.5 g/cm ³	0.40 – 0.60 mm	white
Large Ceramic (P4)	3.8 g/cm ³	0.40 – 0.60 mm	red
Fluid	density ρ	viscosity ν	color
PDMS oil	0.971 g/cm ³	10 ⁻³ m ² /s	clear

mathematical model, χ is independent of space and time. When two densities are present, we define $\chi = \frac{V_g}{V_g + V_c}$, where V_g is the volume of glass beads and V_c is the volume of ceramic beads. When two diameters are present, we define $\chi = \frac{V_l}{V_s + V_l}$, where V_l is the volume of large beads and V_s is the volume of small beads. Recall the total volume fraction $\phi_0 = \frac{V_{\text{particles}}}{V_{\text{total}}}$. In bidensity experiments, $\phi_0 = 0.4$ is constant. We set χ between 0 and 1 in increments of 0.25, and α between 20° and 50° in increments of 10°. The total volume fraction $\phi_0 = 0.3$ is constant in bidisperse experiments. We set χ to 0.20, 0.50, or 0.80, and α to 20° or 30°.

We continually add slurry to the track for constant flux experiments, so we must modify the first steps of the general procedure. To keep the rate consistent, we use a MityFlex 4200 peristaltic pump. Although it is designed for viscous fluid, the flow rate is not constant for different types of slurries. Therefore, we measure the flow rate before every experiment. Additionally, we place an acrylic weir on the track to spread the slurry along the width. We

consider the location of the weir to be the beginning of the flow in our data analysis. Once the slurry flows down the track, we collect data as described in 3.2.

In constant volume experiments, the slurry is poured into a reservoir at the top of the track and then released. There is very little time between placing the slurry on the track and starting the experiment to prevent settling. The beginning of the flow is the location of the gate, which is raised by hand for each experiment.

3.2 Data Analysis

We utilize MATLAB programs to analyze all of the data we collect from our experimental trials. The two primary techniques used are for tracking the front positions and producing a height profile of the slurry as it flows down the track.

All of our experiments use a Canon EOS Rebel T2i camera to record the trials. For front tracking data, the camera is situated in front of the track. The camera lens is tilted to the same degree α as the track so the lens is perpendicular to the track, reducing glare. The camera's view is generally from the 5 cm to 80 cm markers along the track. The slurry is poured either behind a gate or a weir, for constant volume and constant flux, respectively, to designate the starting position of the fluid flow. This starting position is generally at the 5 cm marker along the track.

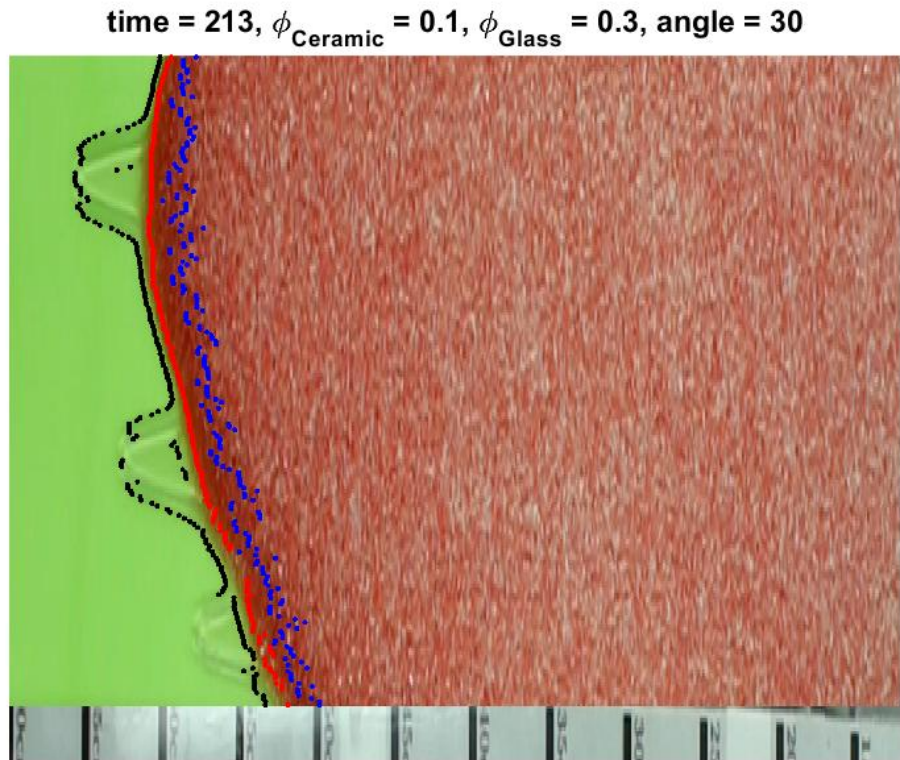


Figure 4: Processed front tracking image.

For front tracking, frames are extracted from the raw video according to guidelines provided by the user. These images are cropped and rotated so only the track and slurry are in the image. The user selects color profiles for each of the fronts, and from each of the profiles, the front position is determined within each frame, and the position data is saved into vectors. From this data, position profiles are plotted, video profiles of the slurry are made, and other plots, such as velocity plots or log plots used to check theory derived values, are additionally computed. Figure 4 shows a processed frame used to produce a video of the experiment.

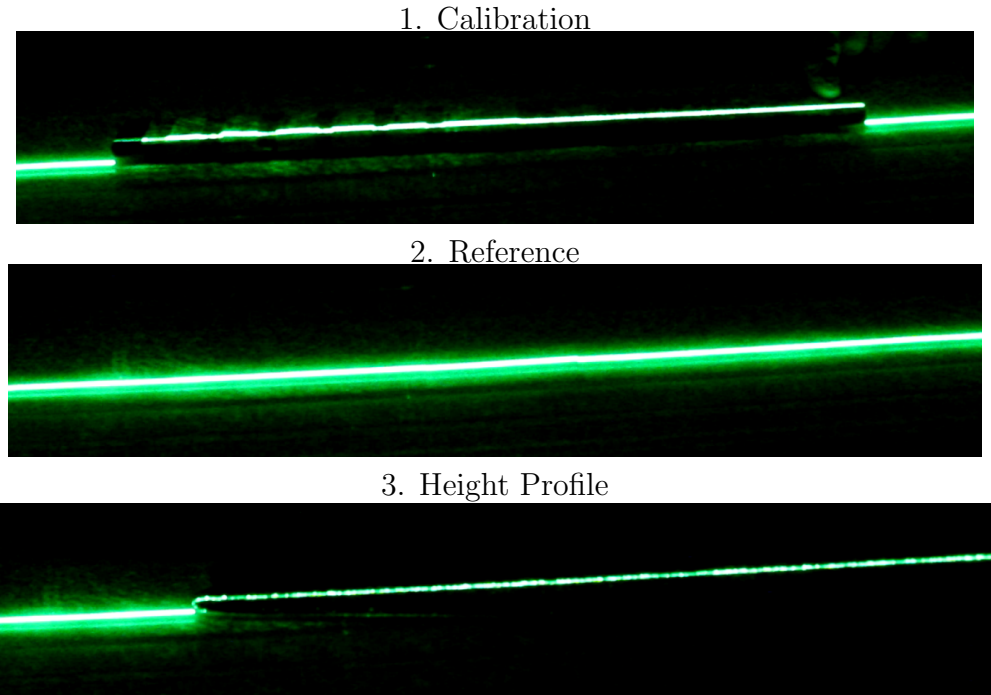


Figure 5: Three frames are analyzed to plot height profile of slurry as it flows down track.

For height profile, the experiment setup is the same as front tracking except the camera is positioned to the left side of the track when looking from the top of the track. The camera is situated to be as horizontally parallel as possible. When this is not possible, the code rotates the image as much as needed to be able to analyze it horizontally. The camera is positioned at an angle so that it is slightly inclined onto the track. The inclination is very minimal so that a height is still obtained in the recording. The camera view is generally from the 30 cm to 80 cm markers along the track, although this varies though experiments due to limitations to position camera. A Class II green laser sheet is used to make a line along the track parallel to the track walls. Experiments are performed with lights off so that the recording obtains the laser light only. A ruler of known height is used for calibration and the reflection of laser line onto the track is used as reference line. The image with the reference line sets a vector for where height is 0 mm for the entire length of the view from the camera. The laser line in the track and slurry reflects the height of the mixture. This line is used to measure the height of the slurry. After calibration and the reference laser line are obtained, height profile analyzes raw frames and plots the height of the laser light in the x -direction. The displacement of the laser line from the reference light to the slurry is calculated, and

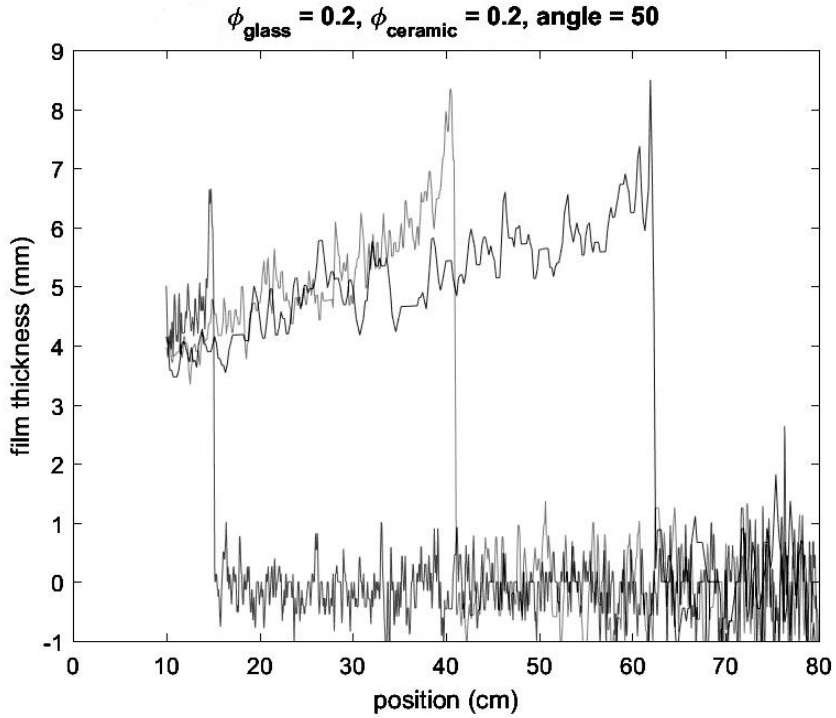


Figure 6: Evolution of the height profile for a ridge regime plot at 42, 2:18 and 3:08 seconds since slurry entered the camera view. In this case, the slurry enters the view of the camera at 15 cm of the track. This is an experiment done at an angle $\alpha = 50$ and $\chi = 0.50$. As it can be seen, height increases in the ridged regime in time.

thus the height along the x -direction is computed. The calibration image with the lights on helps to determine the distortion of distance since the camera is so close to the track, and reverse the effects of this distortion. A height profile of each image extracted from the raw video is produced, and this information is compiled into a video showing the change of height in the x - and z -directions with time.

Both front tracking and height profile have sources of error that we attempt to mitigate. For front tracking, the error primarily comes from the selection of the color profiles used to produce the front position profiles. If the selection of color profiles is too lenient, then portions of the track that are not a part of the fronts will be included in the front position, but if the color profile is too strict, then portions of the front may not be included at all. To relieve this issue, the color profile is selected multiple times to calculate the standard deviation within the front position selection, and produces error bars along the position profile. From this information, it is easier to re-select better color profiles. Additionally, the videos that are produced of the slurry moving down the front are helpful in re-selecting color profiles. Additional errors come from noise, glare, blurs, etc. along the track. These are best dealt with by choosing better cropping and rotating guidelines.

For height profile, errors are mostly generated by reflection of laser line on the track and,

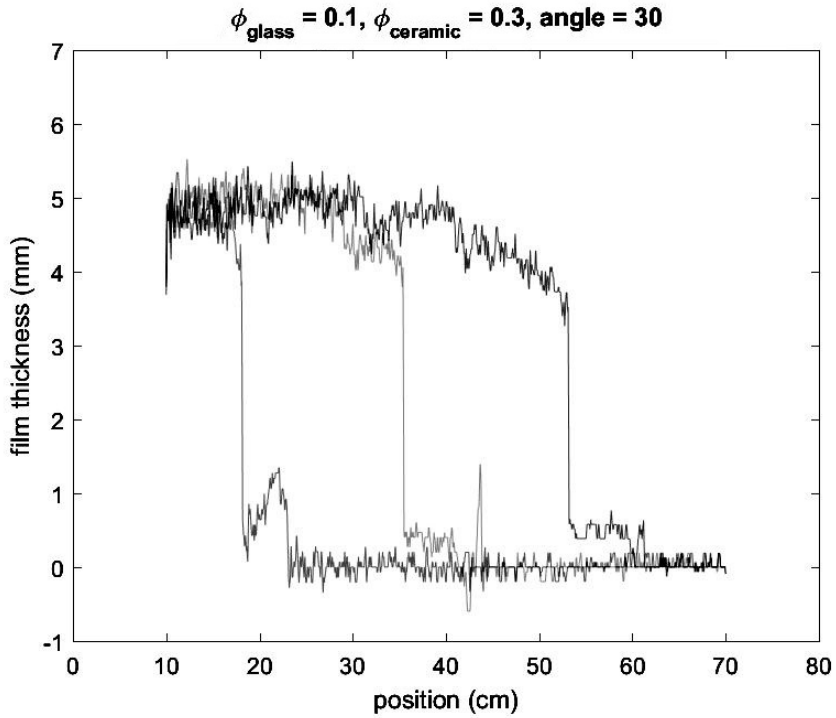


Figure 7: Evolution of the height profile for a settled regime plot at times 3:15, 4:21 and 5:35 minutes since the slurry entered the camera view. In this case, the slurry enters the view of the camera at 10 cm of the track. This experiment consisted of an angle $\alpha = 30$ and $\chi = 0.50$. As it can be seen, height decreases in the settled regime and error is obtained by the plotting of negative height. This is due to the reflection and refraction of the laser line in the track or clear fluid.

in the settled regime, the refraction of the laser line through the transparent PDMS. For the settled regime, the PDMS bends the laser line and hence the frame analysis does not work as desired for this regime. Frames obtained from equivalent intervals from the raw video are saved in a matrix form. The maximum values of this matrix are then saved in a vector together with another vector of their respective index. When the maximum value of this matrix occurs more than once, the index returned is the first occurrence. Due to the method used to obtain position of the laser line, the reflections and refraction of laser in other places besides the desired laser line, the height position being plotted might not always be perfectly correct, but these limitation do not prevent us from getting an accurate height profile.

4 Results

This section will combine experimental and theoretical results from our experiments and simulations. First, we present our results regarding two densities in the slurry, and then we

present our results regarding the presence of two diameters in the slurry.

4.1 Bidensity

The constant flux bidensity experiments are summarized in Figure 8. As the phase diagram shows, we experimentally see the ridged regime at trials displayed by the blue diamonds, the settled regime at trials displayed by black circles, and the well-mixed regime at trials displayed by red circles. The darker shaded region on the table shows where we expect to see more ridged regimes, and the white area is where we expect to see settled regimes. The light gray region in between our ridged and settled experiments is where we see the well-mixed regime. Images of the actual regimes that formed are shown in Table 2.

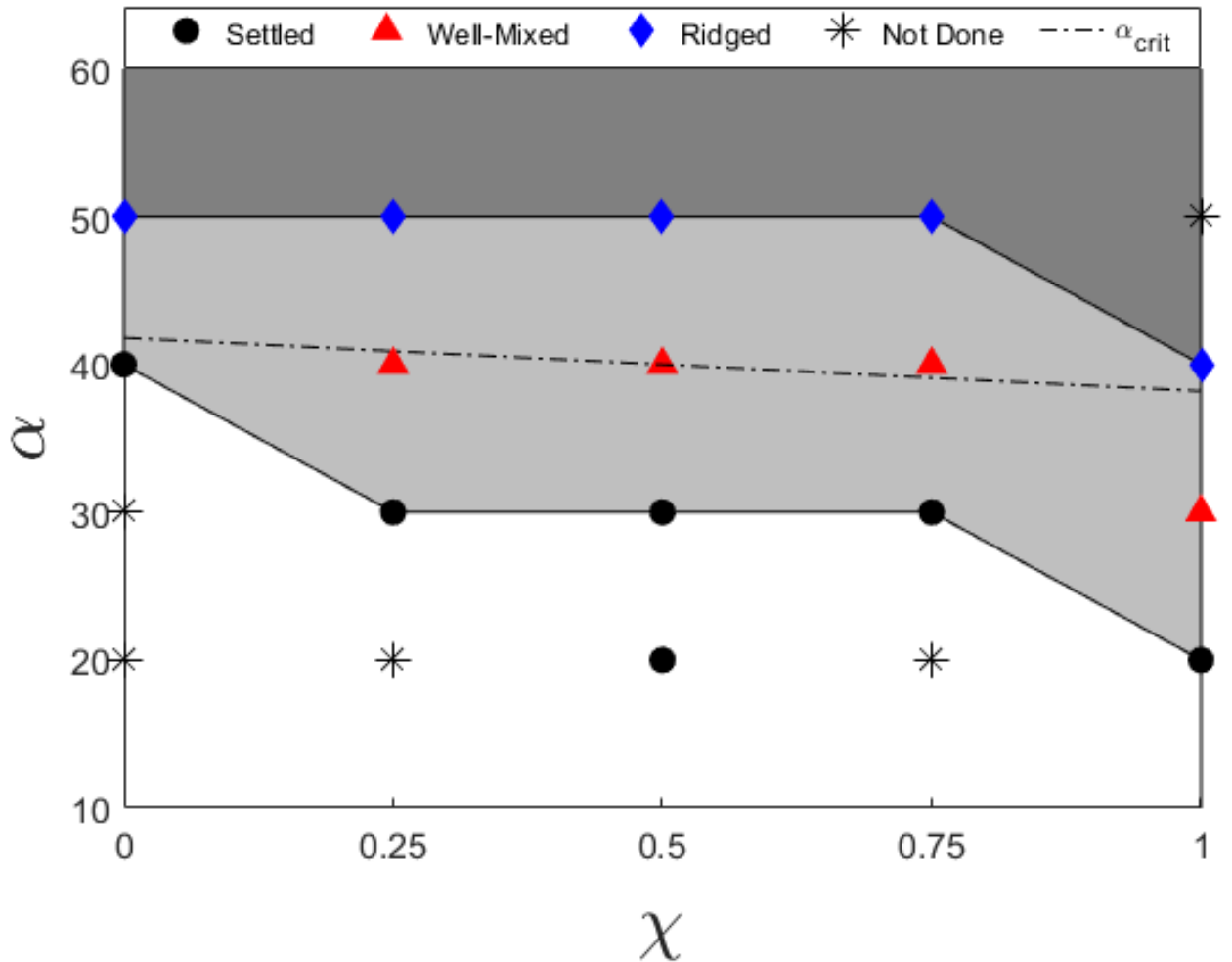


Figure 8: Bidensity Constant Flux Phase Diagram

The dotted line represents a linear fit of the critical angle, α_{crit} . At α_{crit} , the effect of gravitational settling is equivalent to shear induced migration, so the well-mixed regime will result on any time scale. This line is only calculated for the monodisperse cases, $\chi = 0$ and $\chi = 1.0$. The asterisks in the diagram represent trials we did not run. We chose not to run

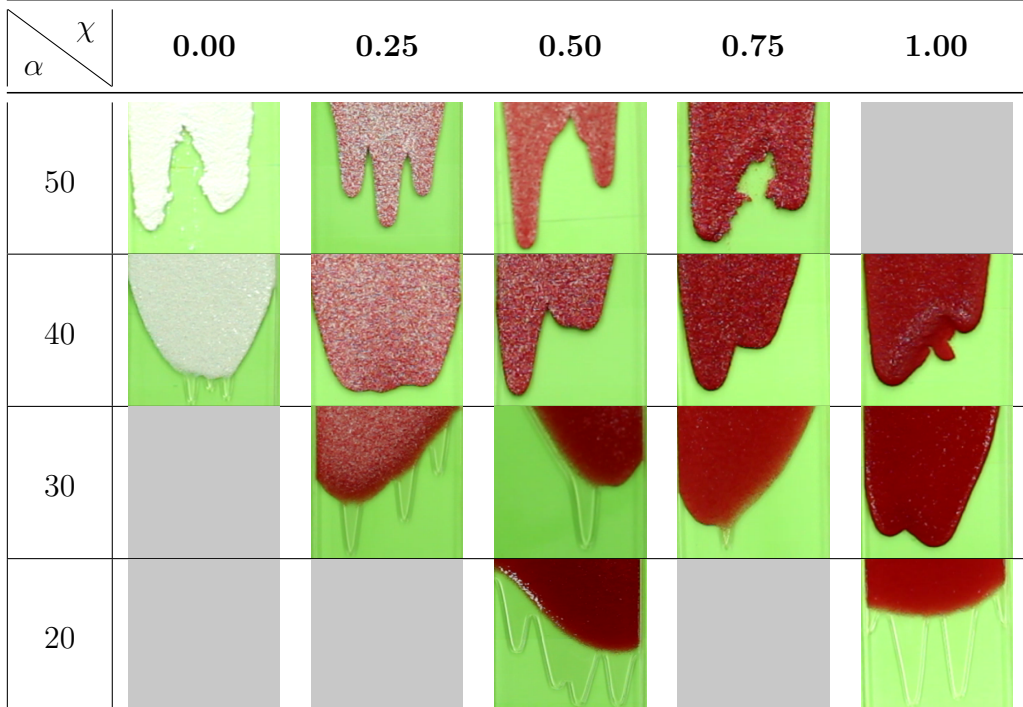


Table 2: Images of all the regimes that formed for each bidensity experiment.

these trials since we already see a regime for an experiment with the same χ value, but with an α closer to α_{crit} , so it is reasonable to expect the same regime to occur.

We see that the our phase diagram is similar to the phase diagram in [8]. Lee et al. performed analogous experiments, but with the constant volume initial condition. In both diagrams, the transition between regimes occurs around $\alpha = 30^\circ$ or 40° , and α_{crit} decreases with χ . However, we note that for constant volume with high χ values, the emergence of the ridged regime does not occur at $\alpha = 40^\circ$, unlike for constant flux.

In addition to the regimes that form for our trials, we are interested in whether the position profile is asymptotic to t^1 as the theory suggests. Table 3 shows all of the exponential values for all fronts from all trials. This table seems to agree quite well with the theoretical t^1 . The mean of all the exponential values is 1.0265 and the standard deviation is 0.05187. The values appear to be quite randomly distributed, that is to say, there are no clear trends within the exponent values with a change in α nor with a change in χ .

We also look into the velocity of the fluid and particle fronts to see if there are reasonable correlations as α and χ change. The velocities of all of these front can not simply be calculated, since there are a range of flow rates for the trials. The pump we use during the constant flux experiments applies a constant amount of well mixed slurry by mass to the track during a unit time, but this value ranges from 1.5 to 2.5 g/s. An experiment that has a faster flow experiences a greater velocity, and an experiment with a slower flow experiences a slower velocity.

To account for this, we attempt to divide the velocity by the mass flow rate, and found these result to be far more consistent. As Figure 9 shows, the $\frac{\text{Velocity}}{\text{Mass Flow Rate}}$ shows an increase for all angles and all front as χ increases, so a greater proportion of glass flows more quickly.

$\alpha \backslash \phi$		0.00	0.25	0.50	0.75	1.00
50	Fluid	1.06	1.01	1.01	1.04	
	Glass		1.07	0.93	1.08	
	Ceramic	1.06	0.99	1.03	1.04	
40	Fluid	1.05	0.99	0.97	1.08	1.05
	Glass		0.95	0.97	1.14	1.06
	Ceramic	1.05	1.01	1.00	1.13	
30	Fluid		0.95	0.95	1.05	1.00
	Glass		0.97	0.99	1.06	1.01
	Ceramic		1.01	1.05	1.06	
20	Fluid			1.11		1.08
	Glass			1.07		1.00
	Ceramic			0.93		

Table 3: This table shows the exponent values of all fluid and particle fronts from every experiment so the values can be compared to theoretical expectations.

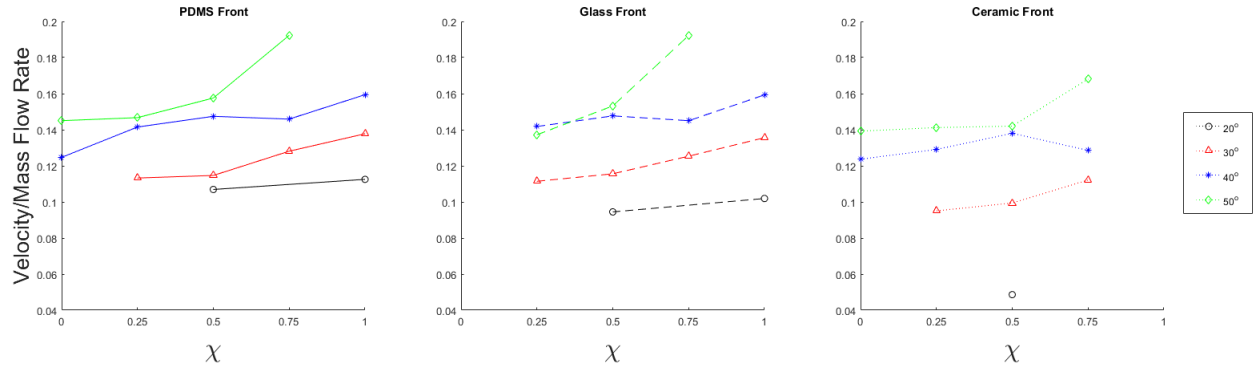


Figure 9: Velocity/Mass Flow Rate vs. Time Plot

This makes sense since the lighter particles stay entrained in the fluid longer and so they would flow down the track faster than heavier particles. Generally, for all experiment, the $\frac{\text{Velocity}}{\text{Mass Flow Rate}}$ also increases with an increasing α . This makes is logical since a large angle would have a greater shear rate, so the particles stay entrained and move faster at the top of the slurry.

In the same way that the velocity profile would benefit from dividing away the mass flow rate, it would be expected that the position profile would benefit from a similar sort of normalization to make the position independent of the mass flow rate. This is less helpful than it may seem in this particular case. The position profiles are not used for any timescale arguments except for possibly a time of onset plot, i.e., a plot showing when the fluid front separates from the particle fronts in the settled experiments. As Figure 10 shows, our experiments have only six settled regimes with at most three trials from the same α value. With so few values, accounting for mass flow rate will not show any special results. Furthermore, even without accounting for mass flow rate, Figure 10 shows the time of onset increasing

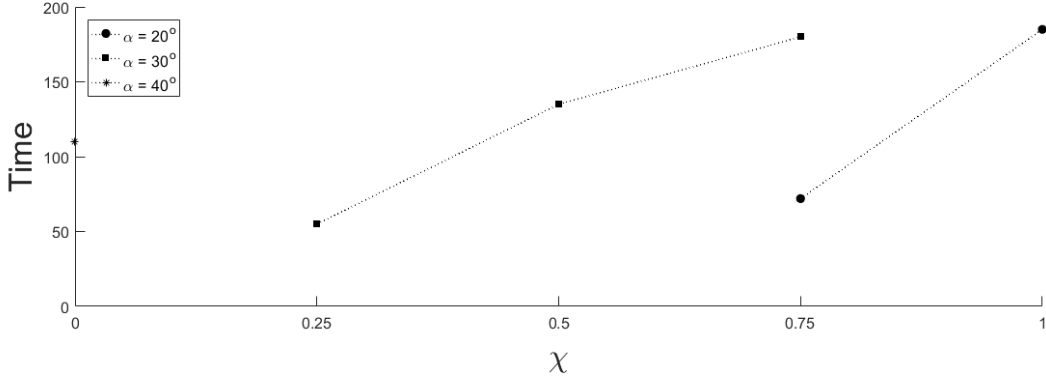


Figure 10: Constant Flux Bidensity Onset Plot

with an increasing α and an increasing χ , similarly to the constant volume bidensity onset plot, so changing the plot for mass flow rate would show no new information [8].

4.1.1 Simulation

In order to produce height profile and front positions, we use finite difference scheme to solve a system of PDEs of three variables h , $\bar{\phi}$ and $\bar{\chi}$. The PDEs have average flux terms f , g_1 , g_2 that depend on $\bar{\phi}$ and $\bar{\chi}$. If we compute these fluxes while running the simulation, it is computationally expensive. Instead, we create flux tables in advance for all the angles we run in our experiments. For each table, we have an array of 300 equally spaced values for $\bar{\phi}$ from 0 to ϕ_m , and also 300 for $\bar{\chi}$ from 0 to 1, and we then evaluate f , g_1 , g_2 at these points.

In our preliminary trials, one thing we notice is that if we choose different tolerance options for `AbsTol` and `RelTol` in `ode15s`, there will be significant changes to our flux plots. For example, the $\alpha = 40^\circ$ case, two different combinations of the tolerances are tried. To save time, we only plot lines for 5 different $\bar{\chi}$ using 20 different $\bar{\phi}$ for each line. Since it is usually g_1 , g_2 that are sensitive to the tolerance options, comparing the plots for $g = g_1 + g_2$ makes sense.

We can see from Figure 11 that using `AbsTol=1e-4`, `RelTol=1e-6` is the better choice. Using `AbsTol=1e-5`, `RelTol=1e-7` produces some noises for $\bar{\chi} = 0.75$.

We do this kind of comparisons in all of our preliminary trials for all angles to choose tolerance options. This does not give us the perfect tolerance combinations as we only do it for 5 different $\bar{\chi}$ and small number of different values of $\bar{\phi}$. The tolerance combinations we choose are,

$$\alpha = 20^\circ, \text{RelTol} = 1e-6, \text{AbsTol} = 1e-8.$$

$$\alpha = 30^\circ, \text{RelTol} = 1e-3, \text{AbsTol} = 1e-6 \text{ for } 0.65 < \bar{\chi} < 0.85;$$

$$\text{otherwise, RelTol} = 1e-5, \text{AbsTol} = 1e-7.$$

$$\alpha = 40^\circ, \text{RelTol} = 1e-4, \text{AbsTol} = 1e-6.$$

$$\alpha = 50^\circ, \text{RelTol} = 1e-3, \text{AbsTol} = 1e-6.$$

When we have the 300×300 tables ready, we first do 3D plots to see whether the surfaces are smooth. Figure 12 is a plot for g_1 for $\alpha = 50^\circ$.

As we can see, there are negative values and many spikes. To fix these, we take three steps. First, we find the positions where negative values occur, and use default tolerance

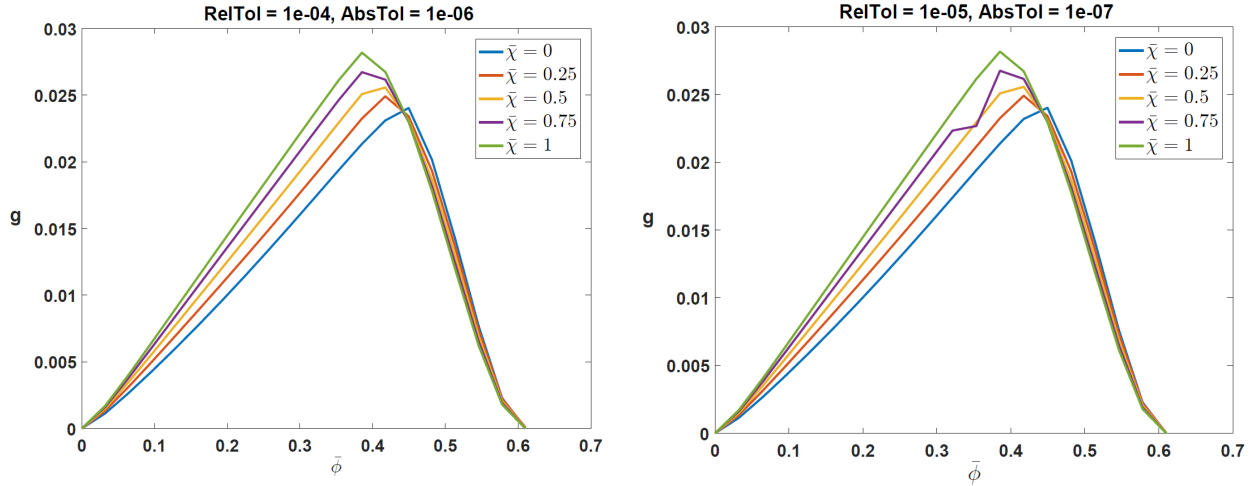


Figure 11: Flux Plots of g with Different Tolerances

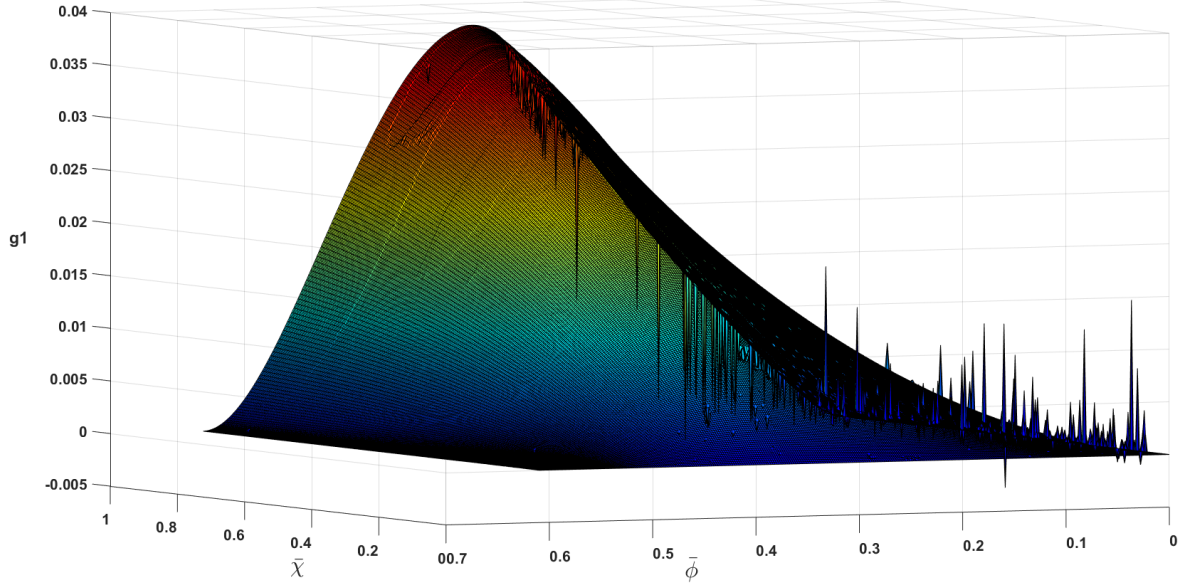
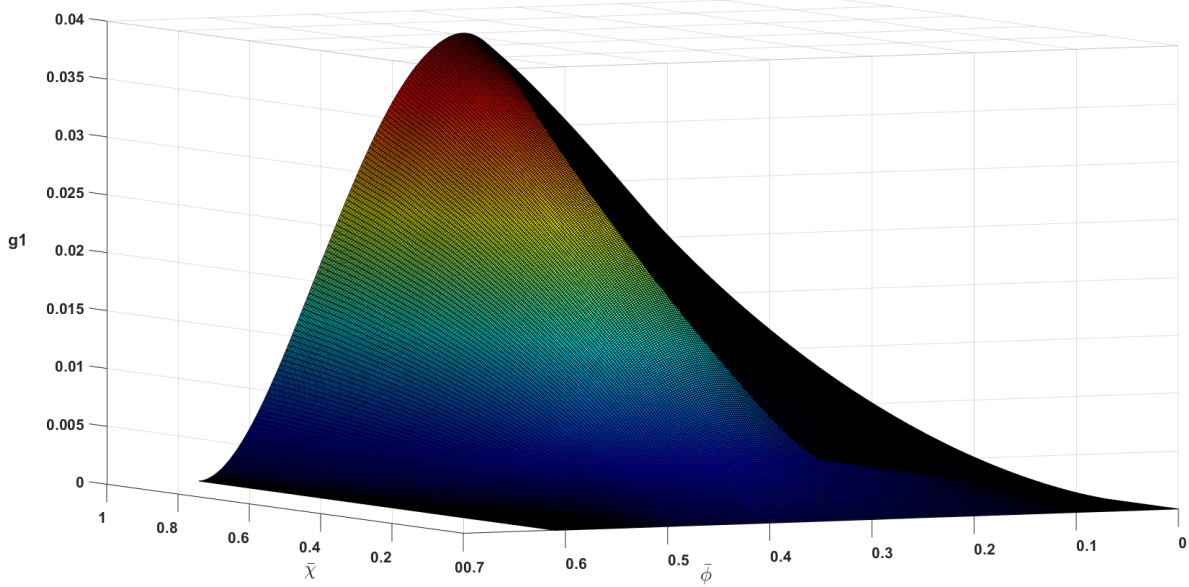


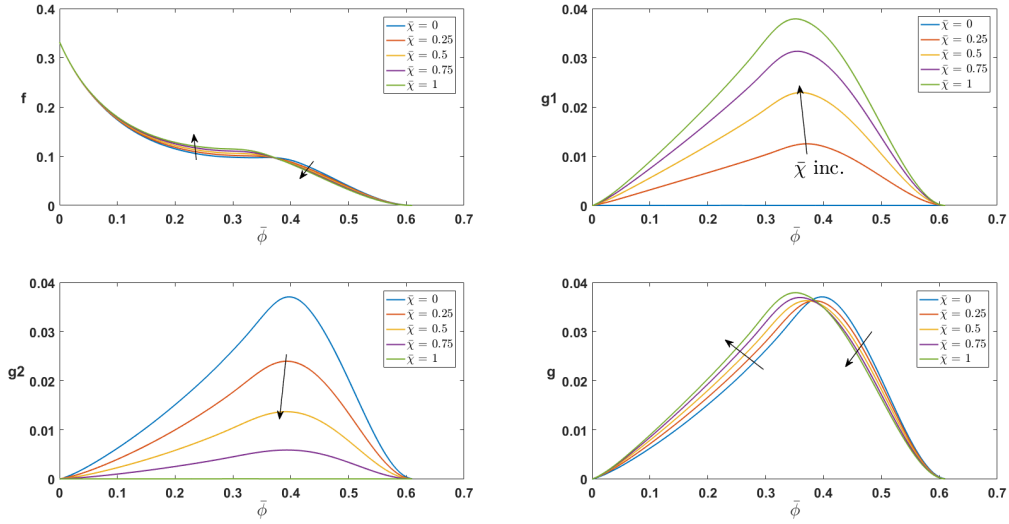
Figure 12: Flux Plot for g_1 , $\alpha = 50^\circ$

option to rerun those values. Next, we detect where those large spikes are, which are usually caused by a single abnormal value. We can try different tolerance options for those abnormal values, but this can be inefficient since we do not know which tolerance combination will actually work. Instead, we do linear interpolation for those points, as we have fine grids and we expect the surface to be smooth. Finally, we use matlab function `sgolayfilt` to further smooth our surface. Figure 13a is the plot for g_1 we get after fixing the negative and abnormal values. We also make similar flux plots as Wong did for $\alpha = 30^\circ$ in [7], for f , g_1 , g_2 as a function of $\bar{\phi}$ using all the 300 points with varying $\bar{\chi} = 0, 0.25, 0.5, 0.75, 1$ at $\alpha = 50^\circ$ in Figure 13b.

As we can see, Figure 13a gives a much better surface plot, and it does not change



(a) Fixed flux plot for g_1 at $\alpha = 50^\circ$

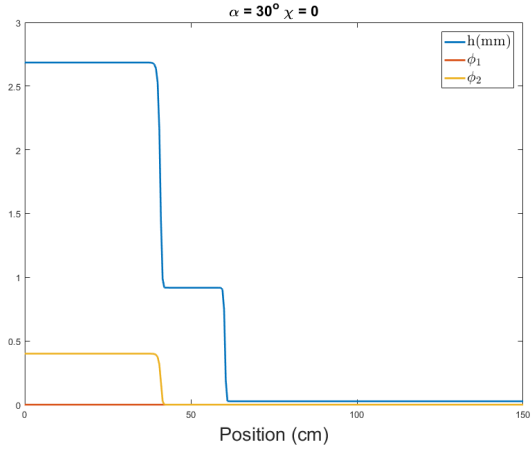


(b) Fixed flux plots of f , g_1 , g_2 as functions of $\bar{\phi}$ for varying $\bar{\chi} = 0, 0.25, 0.5, 0.75, 1$ at $\alpha = 50^\circ$

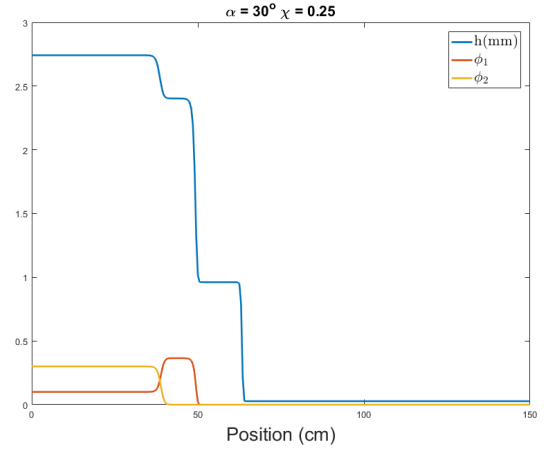
Figure 13: Fixed Flux Plots at $\alpha = 50^\circ$

the general shape of the original plot Figure 12. Also, we observe consistent behavior in Figure 13b with the plots in [7]. We do this modification for all the tables we have.

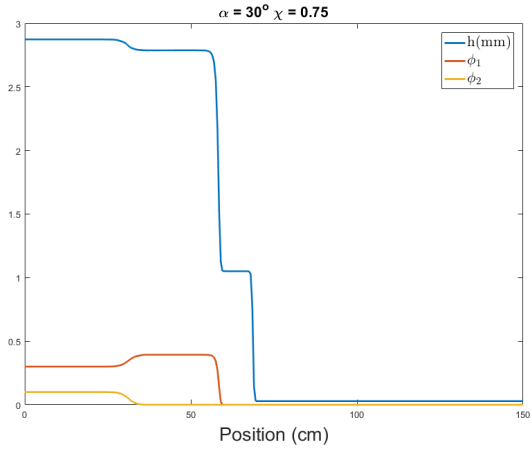
Once we have the tables fixed, we can start running simulations for height profile and front positions. The diagrams in Figure 14a, Figure 14b and Figure 14c correspond to $\alpha = 30^\circ$. And diagrams in Figure 14d, Figure 14e and Figure 14f correspond to $\alpha = 50^\circ$. In Figure 14a when $\chi_0 = 0$, there is only one type of particle in the fluid. So there will be just two shocks corresponding to the clear fluid and the particles. When $\chi_0 \neq 0$, we can see that there are three shocks, corresponding to the clear fluid front, and two particles' front



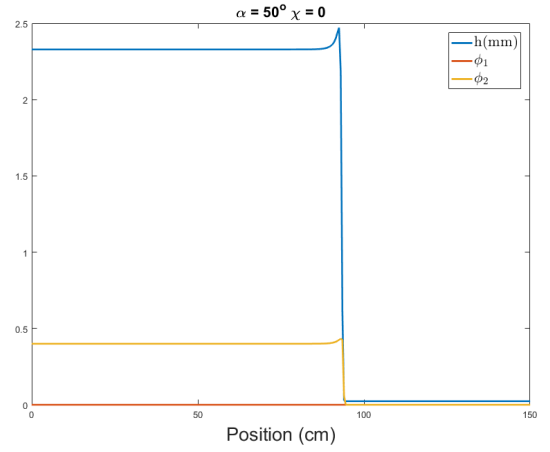
(a) monodisperse, double shocks



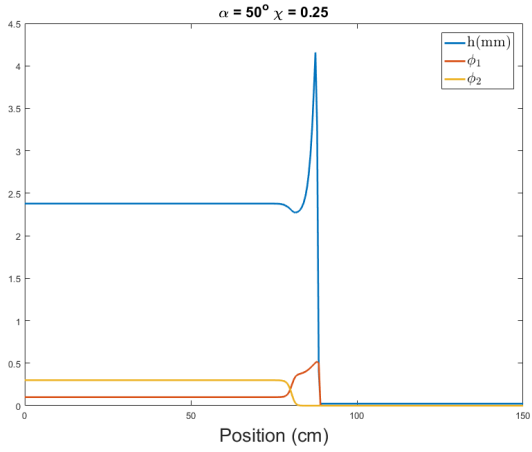
(b) bidensity, triple shocks



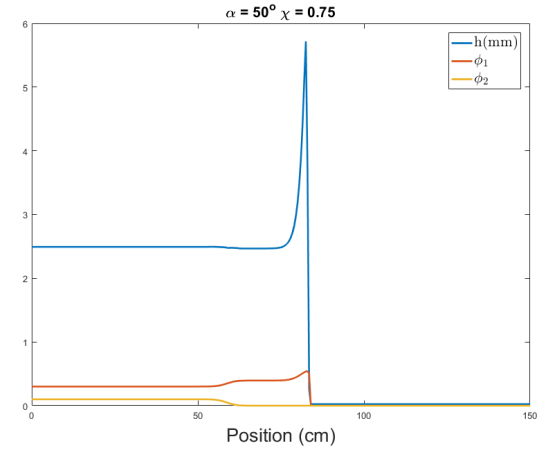
(c) bidensity, triple shocks



(d) monodisperse, ridged regime



(e) bidensity, ridged regime



(f) bidensity, ridged regime

Figure 14: Height profile for different regimes

as shown in Figure 14b and Figure 14c. However, in Figure 14d, Figure 14e and Figure 14f, we observe that a ridged regime has appeared, since there is no clear separation of particles and fluid for all cases. And we can see accumulations of mass at the front of the slurry. Although from the height profile we cannot see multiple shocks, the heavier particle front is still behind the fluid front and lighter particle front by our definition, since in Figure 14e and Figure 14f ϕ_2 already reaches 0 before the spike. In reality, this effect will be more obvious when ϕ_2 is much larger than ϕ_1 in the initial condition. Because all particles in the slurry will be lighter particles after the heavier particle front. If the majority of the particles are heavier particles, then the separation will be more obvious.

To get a sense of how the different components of the slurries are moving, we can look at Figure 16. In the settled regime, there will be three distinct fronts as mentioned before. Hence in the position profile, there are three separate lines indicating three fronts. The gradient of these lines represents the velocities of the three components. In the ridged regime, there are only two lines visible, reason being that the fluid and the lighter particles are moving together and the front positions for them coincide with each other. This is exactly what we would expect from the experiment for the ridged regime. One more important feature in the position profile is the linear relation between position and time for all three components of the slurries, which is expected for the constant flux condition.

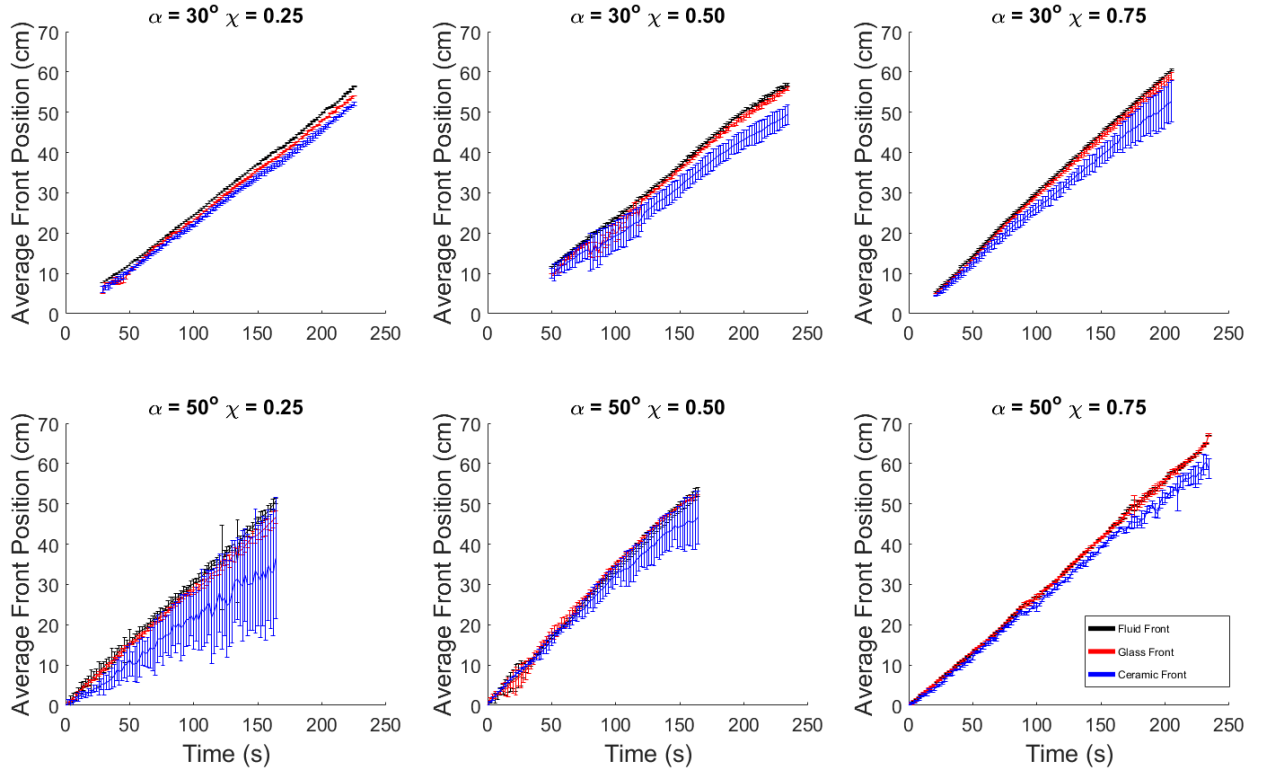


Figure 15: Position profiles of experimental trials $\alpha = 30^\circ$ and $\alpha = 50^\circ$ for $\chi = 0.25$, 0.50 , and 0.75 .

To get a comparison of the front position evolution between the experiments and simulation, we can superimpose the data. The results are shown in Figure 17. In the settled

regime, there are three distinct lines in both simulation and experiment corresponding to the three fronts. Although they do not align perfectly, we can see that qualitatively, the fluid and the lighter particles are behaving similarly to simulation, as they are moving with similar velocity. In the ridged regime, the front position for the fluid and the lighter particle coincide with each other nicely as we have expected. The velocity of the fluid is sometimes underestimated for the experimental data. The reason is that sometimes, the clear fluid separates from the slurry and form a long thin finger leading in front of the slurry. But the code for front tracking may not be able to pick that up. Hence the velocity of the fluid should be faster as it appear on the experimental data. The other hindrance for front tracking to get the position of the heavier particles. There are a lot of noises that is difficult to get rid of when tracking the heavier particle front. As a result, the error bar is considerably larger than that of the lighter particle front and the fluid front, and we the comparison for the heavier particle front is not always as good as those for the fluid front and lighter particle front.

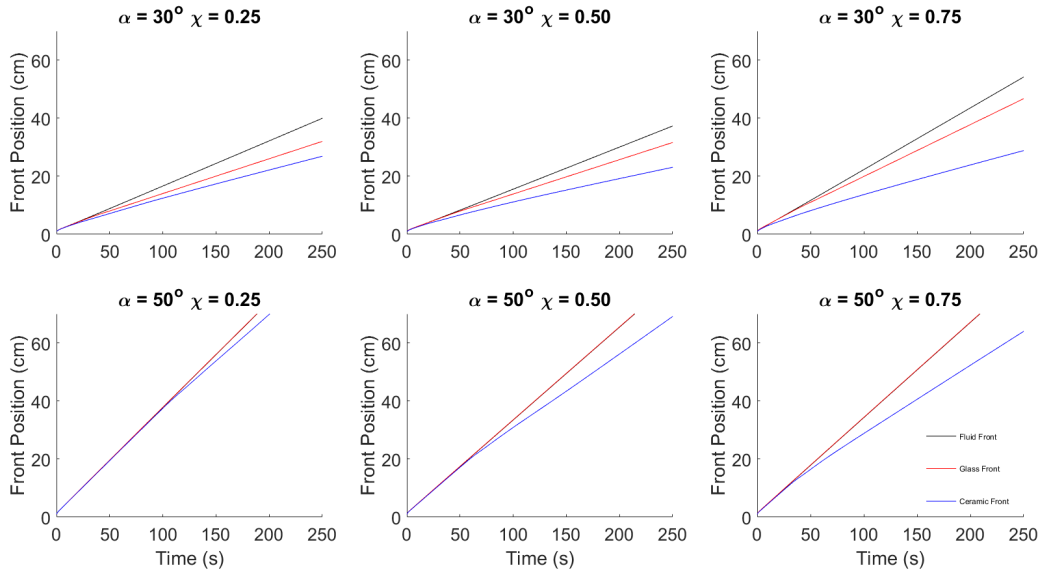
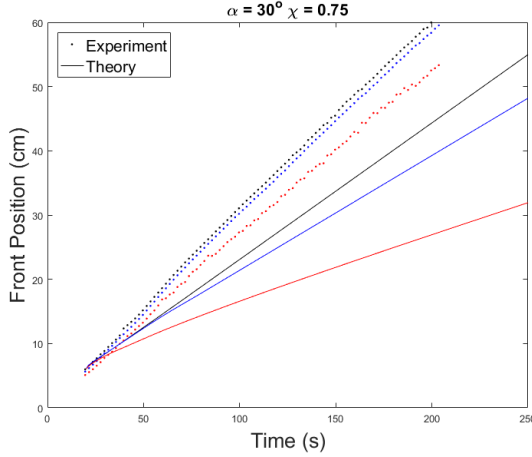
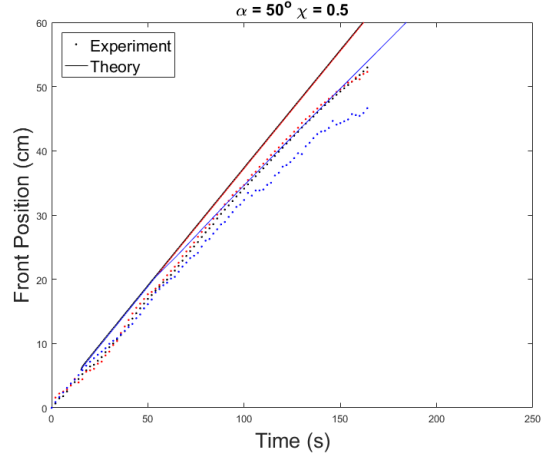


Figure 16: Position profiles of simulations $\alpha = 30^\circ$ and $\alpha = 50^\circ$ for $\chi = 0.25, 0.50$, and 0.75 .

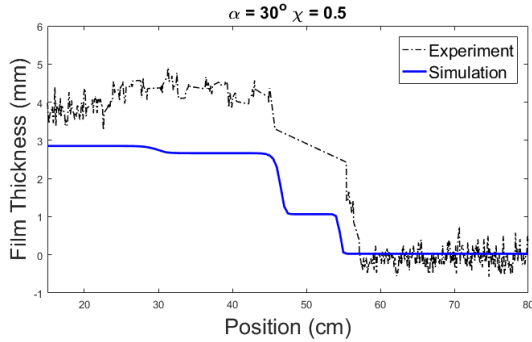


(a) Settled regime, triple shocks.

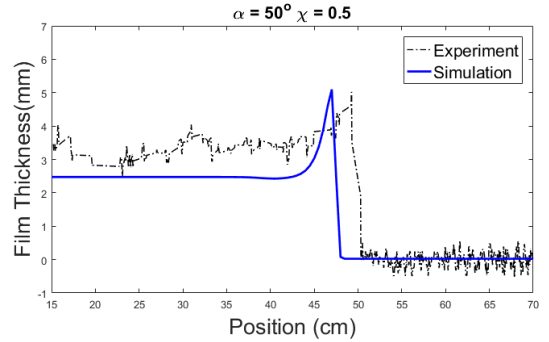


(b) Ridged regime, singular shock.

Figure 17: Front position for different regimes. Black stands for fluid front, red stands for lighter particle front and blue stands for heavier particle front.



(a) Settled regime, triple shocks.



(b) Ridged regime, singular shock.

Figure 18: Height profile for different regimes

The comparison for the height profile is shown in Figure 18. In the settled regime, the height profile for the experimental data and theoretical data correspond to each other well, except that the real height is about 1mm higher than predicted. In the ridged regime, again the shape of the graphs from experiment and simulation agrees with each other. But in the simulation, the spike at the slurry front will keep increasing in height as time goes on. This unrealistic behavior depends on the precursor height for the simulation. In this particular example, the precursor height is set to be 1% of the initial height of the slurry. Higher precursor height will prevent this behavior. If the precursor height is set to be 35% or higher, then the front will not keep getting higher forever.

4.2 Bidisperse

Our results from the bidisperse experiments initially were quite unexpected, primarily since our assumptions of what would occur were based off of the monodisperse diffusive flux

model. For the monodisperse diffusive flux model, all of the fluxes are proportional to the diameter of the particle squared ($\sim d^2$). Thus, time scale arguments are proportional to the inverse of the diameter squared ($\sim d^{-2}$). More specifically, for a particle species with the same density, the time it takes for a slurry to reach its long term regime decreases as the diameter increases. All of our bidisperse experiments investigated settling, so for a monodisperse case, we would see that a larger particle settles more quickly, while a smaller particles settles more slowly. In a bidisperse mixture, without accounting for the affects of collision and shear between particles of different diameter, the immediate expectation would be that the larger particle settle first, then the smaller particles, so behind the fluid front is the smaller particle front, and then the larger particle front.

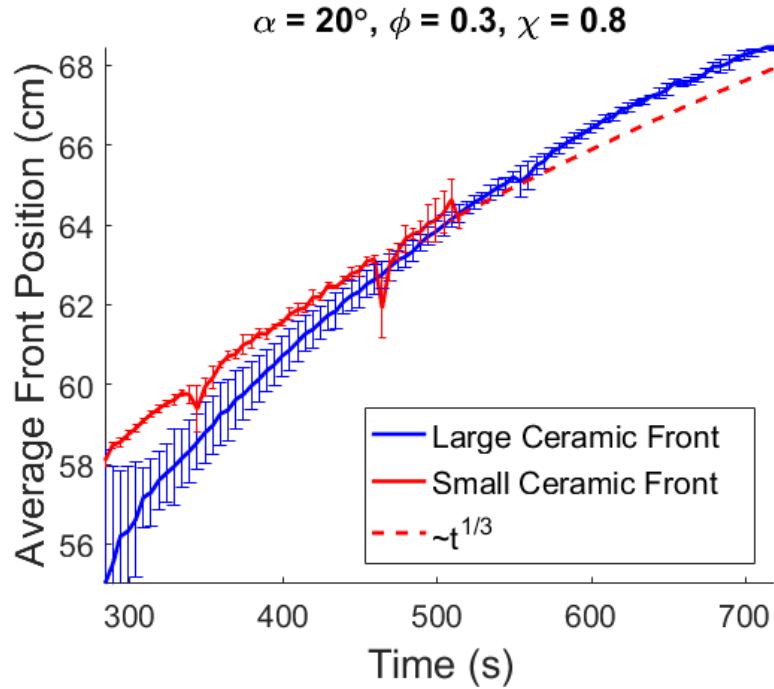


Figure 19: Bidisperse Position Profile

Initially, this is exactly what we see in our bidisperse experiments, but over a long enough time scale, we see the larger particle front migrate in front of the smaller particle front, which the monodisperse diffusive flux model could not account for. Figure 19 shows the position profiles of both ceramic fronts around 300 seconds after the slurry was initially released. As the plot clearly shows, the smaller ceramic front is the first particle front until around 520 seconds after the slurry is released, at which point the larger ceramic front migrates over the small ceramic front. The small ceramic front can no longer be detected by the front tracking code after this phenomenon occurs, but based on the profile prior to the large ceramic front overtaking the small ceramic front, we extrapolate a $t^{1/3}$ fit that indicates that the particle fronts continue to separate with the large ceramic front ahead of the small ceramic front.

Figure 21 shows the fluxes down the track for the bidisperse model, f , g_1 , and g_2 , that we find for the $\alpha = 20^\circ$ case. We don't have accurate values for $\bar{\phi} > 0.5$ due to the shooting method code searching only within the region $[0, 0.61]$ for initial values of ϕ . Because ϕ_m is



(a) Large particle front behind small particle front.
 (b) Large particle front overcame smaller particle front.

Figure 20: Experiment with particles of two different size. Large particle is dyed white and smaller particles are dyed pink.

no longer a constant in the bidisperse model and may be higher than 0.61, the starting value for ϕ may need to be higher than 0.61, which the shooting method code doesn't currently account for. Fixing this issue should be a priority before doing further simulations of the bidisperse model.

From the model we have only a preliminary simulation, but qualitatively the behavior of the simulation appears to agree with the experiments. Figure 22 shows the results of the simulation for $\alpha = 20^\circ$, with initial ϕ and χ values of $\phi = 0.3$ and $\chi = 0.8$. By time 20, the small particles have quickly moved to the front to form a small particle front. But slowly over time, this small particle front starts to spread out and lag behind, while the large particles begin to build up a new front and overtake the small particles. This agrees with what we saw in the experiments, and so at first glance it seems that this model can adequately explain the phenomena observed in the bidisperse experiments.

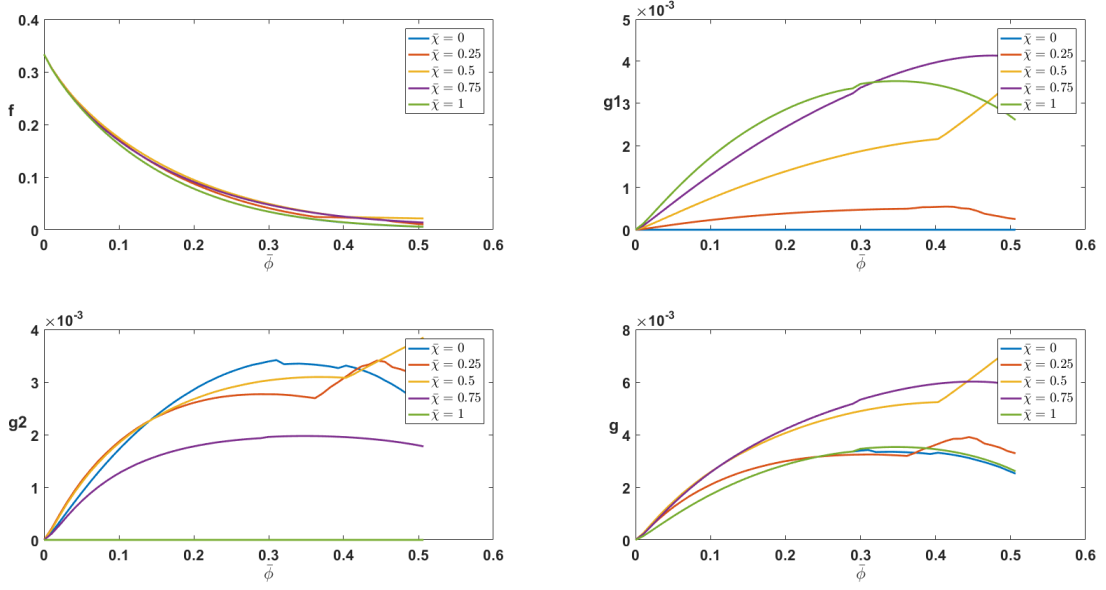


Figure 21: Fluxes in the bidisperse model for $\alpha = 20^\circ$, with X going from 0 to 1 and ϕ from 0 to 0.5.

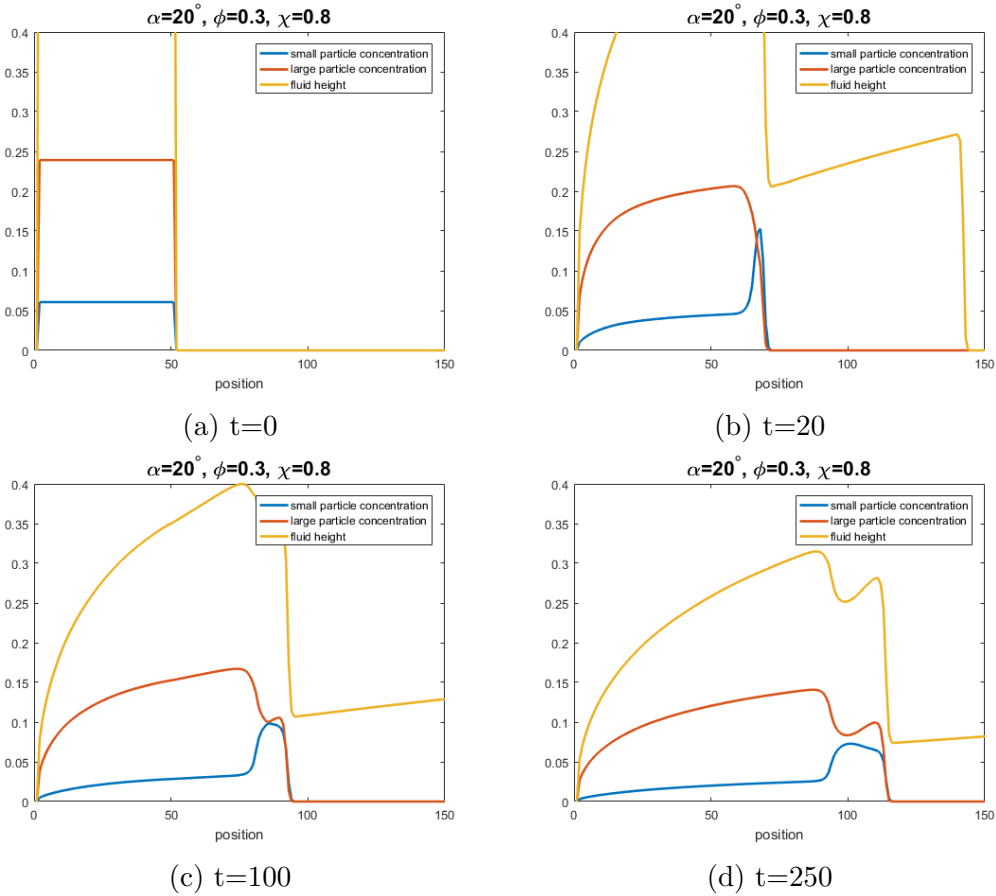


Figure 22: Evolution of the bidisperse model over time

5 Conclusion

In this REU report, we investigate the effects of the constant flux initial condition on bidensity slurries and the constant volume initial condition on bidisperse slurries flowing down an incline and develop new theoretical models together with numerical simulations for comparison. In the constant flux bidensity experiments, we see many similarities to constant volume bidensity slurries, as published in [8]. When we compare our results for the same experimental parameters, we find that the well mixed regime emerges at around $\alpha = 40^\circ$ for both types of initial conditions. Constant flux experimentally experiences the same constriction of the well mixed band at lower χ values, while the settled regime portion increases.

In addition to similarities to constant volume bidensity, we see correlation between experimental bidensity data and numerical simulations we have developed. The height profile in Figure 18 shows a similar shape in the experiment and simulation for both ridged and settled regime, although there is a 1 mm difference in height. The front position profile is not ideal but we do observe some qualitative consistency between the experiment and the simulation. Improved techniques should be employed in the future to obtain a better height profile tracking.

In our bidisperse investigations, we discover a new settling phenomenon and produce a new theoretical model to better explain our results. We see that with enough time, a larger particle front will be behind a small particle front and eventually overcome the smaller particle front, which is unexpected since it does not correlate to results in [5]. Murisic et al. found that large beads take less time to settle than small beads, which would indicate that the large particle front would cease to move before a small particle front does. We create a bidisperse model, which qualitatively displays the behavior that we observe, but more investigation needs to be done to then make comparisons between experimental data and model.

We suggest future work on particle laden flow, especially for the settled regime in the bidisperse case. While constant flux bidensity slurries closely paralleled constant volume bidensity experiments, there is little investigation done for constant flux bidensity slurries that occur at a lower volume fractions. The case should be compared to its constant volume counterpart. Additionally, there has yet to be any investigation into constant flux bidisperse slurry flow down an incline for different diameters.

For constant volume bidisperse, there is still more investigations required to explain the settling phenomenon. This will then allow us to update our theoretical model. There are also the well mixed and ridged regimes that need to be explored together with bidisperse diffusive flux model, which can then be compared to the monodisperse constant flux model.

6 Acknowledgements

We would like to express our gratitude to Professor Andrea Bertozzi, Professor Marcus Roper, and our mentor, Professor Claudia Falcon for their guidance. Additionally, we thank Professor David Arnold and Professor Mike Lindstrom for their advice. We acknowledge financial support from the NSF grants DMS-1312543 and DMS-1659676.

References

- [1] Herbert E Huppert. Flow and instability of a viscous current down a slope. *Nature*, 300(5891):427–429, 1982.
- [2] D. Leighton and A. Acrivos. The shear-induced migration of particles in concentrated suspensions. *Journal of Fluid Mechanics*, 181:415–439, August 1987.
- [3] R. J. Phillips, R. C. Armstrong, R. A. Brown, A. L. Graham, and J. R. Abbott. A constitutive equation for concentrated suspensions that accounts for shear-induced particle migration. *Physics of Fluids A*, 4:30–40, January 1992.
- [4] B. P. Cook. Theory for particle settling and shear-induced migration in thin-film liquid flow. *Physical Review E*, 78(4):045303, October 2008.
- [5] N Murisic, J Ho, V Hu, P Litterman, T Koch, K Lin, M Mata, and AL Bertozzi. Particle-laden viscous thin-film flows on an incline: Experiments compared with a theory based on shear-induced migration and particle settling. *Physica D: Nonlinear Phenomena*, 240(20):1661–1673, 2011.
- [6] N. Murisic, B. Pausader, D. Peschka, and A. L. Bertozzi. Dynamics of particle settling and resuspension in viscous liquid films. *Journal of Fluid Mechanics*, 717:203–231, 2013.
- [7] Jeffrey T. Wong and Andrea L. Bertozzi. A conservation law model for bidensity suspensions on an incline. *Physica D. Nonlinear Phenomena*, 330:47–57, 2016.
- [8] Sungyon Lee, Aliki Mavromoustaki, Gilberto Urdaneta, Kaiwen Huang, and Andrea L Bertozzi. Experimental investigation of bidensity slurries on an incline. *Granular Matter*, 16(2):269–274, 2014.
- [9] Gladstone, Phillips, and Sparks. Experiments on bidisperse, constant-volume gravity currents: propagation and sediment deposition. *Sedimentology*, 45:833–843, October 1998.
- [10] Anat Shauly, Amir Wachs, and Avinoam Nir. Shear-induced particle resuspension in settling polydisperse concentrated suspension. *International journal of multiphase flow*, 26(1):1–15, 2000.
- [11] Andre Pradhana Tampubolon, Theodore Gast, Gergely Klár, Chuyuan Fu, Joseph Teran, Chenfanfu Jiang, and Ken Museth. Multi-species simulation of porous sand and water mixtures. *ACM Transactions on Graphics (TOG)*, 36(4):105, 2017.
- [12] Anubhav Tripathi and Andreas Acrivos. Viscous resuspension in a bidensity suspension. *International journal of multiphase flow*, 25(1):1–14, 1999.
- [13] Samila Bandara, Alessio Ferrari, and Lyesse Laloui. Modelling landslides in unsaturated slopes subjected to rainfall infiltration using material point method. *International Journal for Numerical and Analytical Methods in Geomechanics*, 40(9):1358–1380, 2016.

Appendix A Toy Problem

One assumption that we make in the bidensity and bidisperse models is that in the z -direction, the concentration equilibrates much faster than in the x -direction. This allows us to assume that the total flux in the z -direction is always equal to 0, which leads to the model where we first calculate concentration in the z -direction using the system of ODEs and then calculate the flux down the incline in the x -direction. As mentioned in [7], if we do the nondimensionalization of the flow equation we find that a sufficient condition for this assumption to hold is that $\varepsilon \ll (d/H)^2 \ll 1$. However, this condition may not actually be true, and we don't know how good the z -equilibrium approximation is.

To investigate what happens in a system where we don't assume motion in the z -direction occurs on a much smaller time scale than in the x -direction, we look at a simplified mathematical model. This model, which we call the “toy problem,” consists of two coupled partial differential equations for $u(x, z, t)$, which represents the velocity in the x -direction, and $\phi(x, z, t)$, which represents the concentration:

$$u_{zz} = -1 + \phi$$

$$\phi_t + \eta(u\phi)_x = \varepsilon\phi_{zz}$$

The boundary conditions are

$$u(z=0) = 0$$

$$u_z(z=1) = 0$$

$$\phi_z(z=0) = \phi_z(z=1) = 0$$

This model includes both advection in the x -direction and diffusion in the z -direction. The boundary conditions for ϕ ensure that there is no flux in or out at the z -boundaries, while for u the two boundary conditions are a no-slip condition at the bottom and a no-stress condition at the top.

We can solve the toy problem using a finite difference scheme that is implicit in z while using the upwind scheme in x . The scheme is created using the following finite difference equation in ϕ_{mp}^n , where n is the time index, m the spatial index in the x -direction, and p the spatial index in the z -direction:

$$\frac{\phi_{mp}^{n+1} - \phi_{mp}^n}{k} + \eta \frac{u_{mp}^n \phi_{mp}^n - u_{m-1,p}^n \phi_{m-1,p}^n}{h} = \varepsilon \frac{\phi_{m,p+1}^{n+1} - 2\phi_{mp}^{n+1} + \phi_{m,p-1}^{n+1}}{l^2}.$$

The flux in the x -direction is approximated with a backwards-space scheme at the old time step. But the diffusion in the z -direction is approximated at the new time step, so it has to be solved implicitly.

Define

$$f_{mp}^n = \eta \lambda \frac{u_{mp}^n \phi_{mp}^n - u_{m-1,p}^n \phi_{m-1,p}^n}{h},$$

the flux in the x -direction. Then if we rearrange the finite difference equation, we get

$$-\varepsilon\mu\phi_{m,p+1}^{n+1} + (1 + 2\varepsilon\mu)\phi_{mp}^{n+1} - \varepsilon\mu\phi_{m,p-1}^{n+1} = \phi_{mp}^n - f_{mp}^n.$$

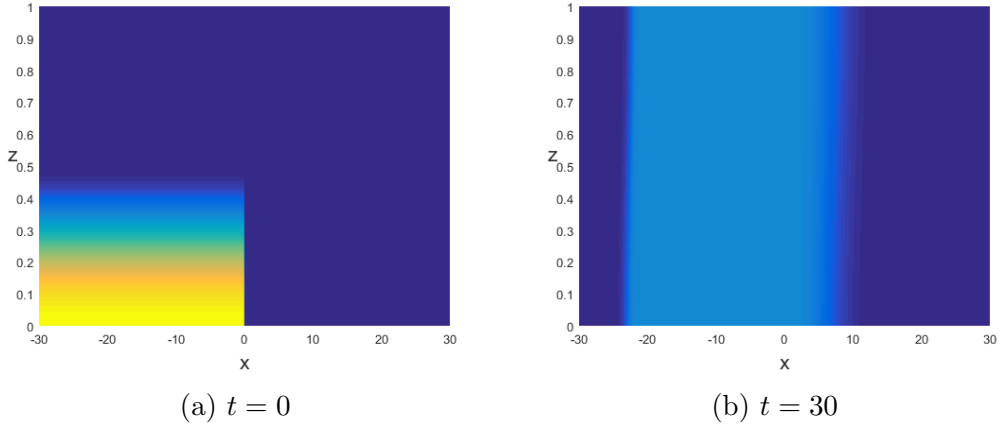


Figure 23: Result of the numerical simulation of the toy problem

This is the system of linear equations we have to solve. But the above equation doesn't work at the boundaries. If the boundaries for p are $1 \leq p \leq N$ then the above equation is only valid for $2 \leq p \leq N - 1$. To get the two boundary conditions, we use the fact that the total ϕ in the z -direction should be conserved; that is, there should be no flux in or out at the z -boundaries. We find that to conserve the total concentration, we want the two boundary conditions

$$\phi_{m1}^{n+1} = \frac{\varepsilon\mu}{1 + \varepsilon\mu} \phi_{m2}^{n+1} + \frac{1}{1 + \varepsilon\mu} (\phi_{m1}^n - f_{m1}^n)$$

and

$$\phi_{mN}^{n+1} = \frac{\varepsilon\mu}{1 + \varepsilon\mu} \phi_{m,N-1}^{n+1} + \frac{1}{1 + \varepsilon\mu} (\phi_{mN}^n - f_{mN}^n).$$

To find the stability of the scheme in the z -direction, we take the Fourier transform:

$$\begin{aligned} \tilde{\phi}^{n+1} - \tilde{\phi}^n &= \varepsilon\mu \tilde{\phi}^{n+1} (e^{il\zeta} - 2 + e^{-il\zeta}) \\ \tilde{\phi}^{n+1} (1 + 2\varepsilon\mu - \varepsilon\mu (e^{il\zeta} + e^{-il\zeta})) &= \tilde{\phi}^n \end{aligned}$$

So the amplification factor of the scheme is

$$g = (1 + 2\varepsilon\mu(1 - \cos \varphi))^{-1} = (1 + 4\varepsilon\mu \sin^2(\varphi/2))^{-1}.$$

Since $|g|^2 < 1$ for all values of μ , this scheme is unconditionally stable, which is good. In the x -direction we have an upwind scheme, so the stability is given by the CFL condition, requiring $\eta\lambda u < 1$.

When we run the simulation, we find that it does behave in the way we expect for appropriate values of η and ε . The output of the simulation for $\eta = 1$ and $\varepsilon = 0.05$ is shown in Figure 23. The value ϕ quickly equilibrates in the z -direction and then moves to the right in the x -direction, which is the same behavior that we assume in the slurry flow.

Here it is difficult to study the existence and uniqueness problem for the initial value problem. But we will start by looking into properties of the solution.

First, if η is zero, the second equation becomes a heat equation, with $(x,z) \in (-\infty, +\infty) \times (0,1)$ and $t \geq 0$. We can express the solution in the form of Fourier series. Since now the equation

does not contain derivatives of x , we fix x and $\phi(t,x,z)$ is a function on $(t,z) \in (0,+\infty) \times (0,1)$. Due to the completeness of triangular functions, we set

$$\phi(t, x, z) = \sum a_{k,x}(t) \cos(k\pi z)$$

considering the boundary condition $\phi_z = 0$ on $z=0$ and $z=1$. Substituting the series expansion in the equation, we get $a_{k,x} = C_{k,x} \exp(-\varepsilon k^2 \pi^2 t)$. Using the initial value $\phi_0(x, z) = \phi(0, z, x)$, $C_{k,x} = 2 \int_0^1 \phi_0(x, z) \cos(k\pi z) dz$. In this special case, the bigger ε is, the faster it will obtain relative stability over time.

Appendix B Concentration Measurements

A new experimental technique was developed for the purpose gaining information regarding particle concentration in the track in the x position.



Figure 24: Experiment for concentration measurements in the settled regime. This slurry contains transparent particles and three percent of them are dyed red. Buoyant particles are dyed blue, which can be clearly detected through image processing methods.

. The experimental technique consists of using transparent mono-disperse particles with a small percentage of them dyed in a different color, such as red or blue. We focus on obtaining a settled regime for the purpose of optimizing the spreading of the colored particles, hence we keep experiments at a low angle α and total concentration ϕ . Particles are then be counted in the x -axis and comparisons can be made of the amount of particles in the x position intervals.

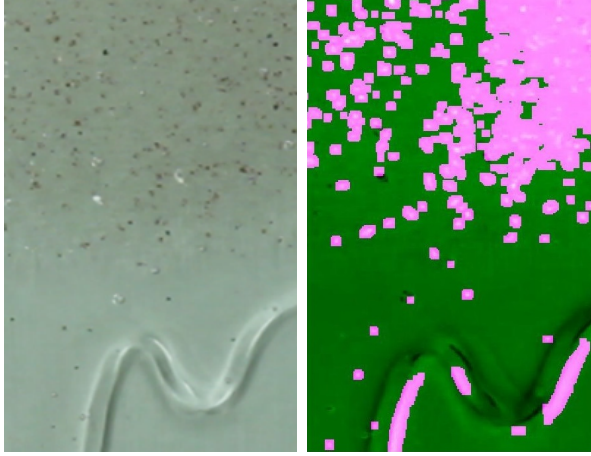


Figure 25: Settled Regime with clear glass particles and three percent dyed red. Image on the right is a preliminary processed image in the attempt to count particles for perspective frame.

Another aspect of this experimental technique is adding buoyant particles to the slurry as it flows down the track. This will allow us to know the position of particle in the top layer of the track and therefore we can obtain the surface speed of the slurry. The frames obtained from this experiments will be analyzed using image processing such a template matching.

This could also give insight as to where the particles are in the z -axis, since we can compute the position in the z -axis using shear induced migration theory. We can compute where in the z -axis a particle is most likely to be after velocity of particle is obtained. A speed vector field can be obtained using particle tracking velocimetry.

Appendix C Landslide Erosion Experiments

Inspired by [11], we develop a series of gravity driven landslide experiments with wet beads. We compare how our ceramic beads mixed with oil compare to Tampubolon et al.’s series of simulations with porous sand and water mixtures. In all experiments, liquid is poured behind a mound of wet beads on a track at angle 20° . We use ceramic beads with diameter $0.125 - 0.250$ mm and density 3.8 g/cm^3 , moistened with PDMS oil ($\rho_f = 0.971 \text{ g/cm}^3$ and $\nu = 10^{-3} \text{ m}^2/\text{s}$). We find experimentally that to form a retaining wall, 5-10% of the mound must be oil by mass.

In the experiment shown in Figure 26, we prepare a retaining wall of height 1.5 cm. The ceramic beads are dyed pink to contrast with the white acrylic track. 6.22% of the mound is oil. The oil accumulates and then flows over the mound. As shown in the image provided, the oil permeates the mound from all sides, primarily from the top. When the oil flows over the mound, erosion occurs, resulting in a fine layer of beads on the track. 19 seconds after the start of the experiment, a large clump is eroded. This results in bubbles forming in that location, beginning 25 seconds from the start of the experiment, as shown in the figure. The final stages of this experiment are similar to Tampubolon et al.’s 2D simulated dam breach series of images with the reversible term from [13]. The initial stages are distinct, primarily because the oil permeates the mound at a significantly slower rate than the simulation.

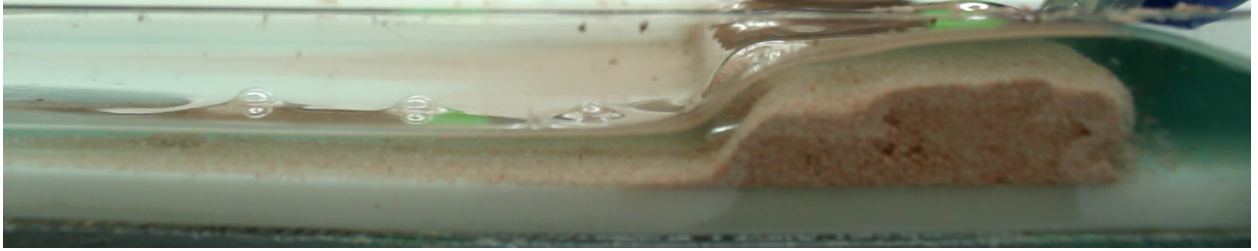


Figure 26: Dam breach experiment with low retaining wall, taken at 38 seconds from the start of the experiment.

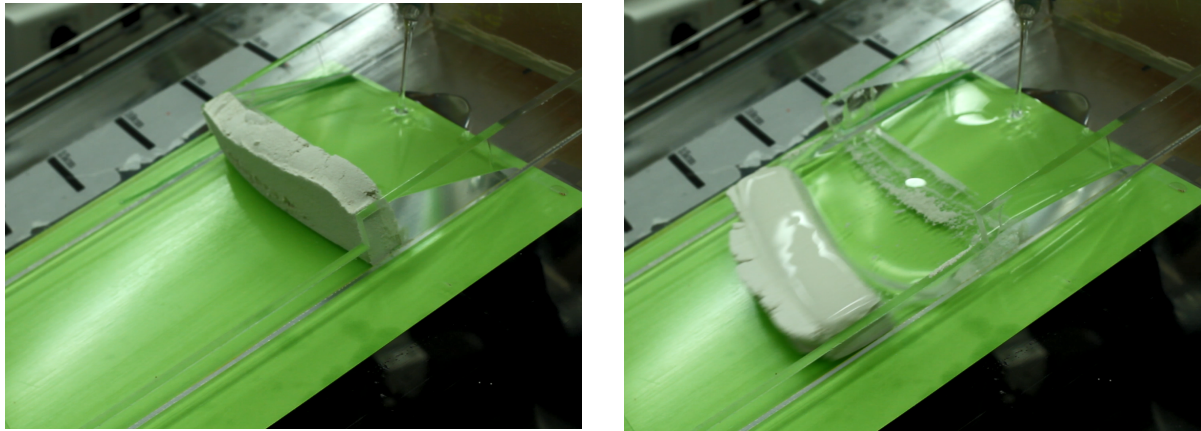


Figure 27: Levee break experiment with high retaining wall, taken 32 seconds and 33 seconds from the start of the experiment, respectively.

In the experiment shown in Figure 27, we prepare a retaining wall of height 3 cm. The mound is 7.68% oil. At first, the oil accumulates behind the retaining wall. Close inspection of the mound next to the transparent wall shows that the oil permeates the retaining wall. Though it is hard to see in the images provided, the video of this experiment reveals that the oil first accumulates behind the wall, and then begins to permeate it. The oil permeates the top of the mound at a faster rate than the bottom. The wall begins to bend down the track at 21 seconds and collapses at 33 seconds into the experiment. Unlike the series of levee break images in [11], the oil does not permeate the wall. Rather, the wall falls forward in one piece and the oil flows over the fallen mound.